

Incorporating a radiative hydrodynamics scheme in the numerical-relativity code BAM

Henrique Gieg^{1,*} , Federico Schianchi² , Tim Dietrich^{3,4} , Maximiliano Ujevic⁵ 

¹ Centro de Ciências Naturais e Humanas, Universidade Federal do ABC, 09210-170, Santo André, São Paulo, Brazil; henrique@gieg.com.br

² Institut für Physik und Astronomie, Universität Potsdam, Haus 28, Karl-Liebknecht-Str. 24/25, 14476, Potsdam, Germany; schianchi@uni-potsdam.de

³ Institut für Physik und Astronomie, Universität Potsdam, Haus 28, Karl-Liebknecht-Str. 24/25, 14476, Potsdam, Germany; tim.dietrich@uni-potsdam.de

⁴ Max Planck Institute for Gravitational Physics (Albert Einstein Institute), Am Mühlenberg 1, Potsdam 14476, Germany; tim.dietrich@aei.mpg.de

⁵ Centro de Ciências Naturais e Humanas, Universidade Federal do ABC, 09210-170, Santo André, São Paulo, Brazil; mujevic@ufabc.edu.br

* Correspondence: henrique@gieg.com.br

Abstract: To study binary neutron star systems and to interpret observational data such as gravitational-wave and kilonova signals, one needs an accurate description of the processes that take place during the final stages of the coalescence, e.g., through numerical-relativity simulations. In this work, we present an updated version of the numerical-relativity code BAM in order to incorporate nuclear-theory based Equations of State and a simple description of neutrino interactions through a Neutrino Leakage Scheme. Different test simulations, for stars undergoing a neutrino-induced gravitational collapse and for binary neutron stars systems, validate our new implementation. For the binary neutron stars systems, we show that we can evolve stably and accurately distinct microphysical models employing the different equations of state: SFHo, DD2, and the hyperonic BHB $\Lambda\phi$. Overall, our test simulations have good agreement with those reported in the literature.

Keywords: Numerical Relativity; Binary Neutron Stars; Neutrinos; Leakage Scheme

1. Introduction

In August 2017 the Advanced LIGO [1] and Advanced Virgo [2] gravitational-wave (GW) interferometers detected for the first time a GW signal arising from the merger of two neutron stars (NSs) (GW170817) [3]. This GW detection was accompanied by a variety of electromagnetic (EM) signatures across the entire frequency spectrum [4]. The observed signals, GWs and EM, were created by a binary neutron star (BNS) merger that happened about 130 million years ago in the galaxy NGC 4993 [4]. While the GW signal was emitted during the inspiral of the stars before the merger, the EM signals were created after the merger. These include the short gamma-ray burst GRB170817A [5] observed 1.7 seconds after the stars collision, the weeks-long kilonova AT2017gfo [6–11], and sGRB/kilonova afterglows that are still observable [12,13].

Over the last years, this landmark discovery was extensively studied and yielded constraints not only on the NS properties, such as radius, tidal deformability, and its Equation of State (EoS) [14–27], but also on the expansion rate of our Universe [25,28–34]. However, we still have not fully understood the internal NS structure, the composition and the underlying physics since many modelling aspects are plagued by large uncertainties.

Indeed, for a correct interpretation of the observables, one has to correlate the observational data with theoretical predictions. For the development of such models, numerical-relativity (NR) simulations are an important prerequisite as they provide a testbed for new GW models,



e.g., [35] and references therein, and they enable us to connect properties of the outflowing matter to the binary properties [22,23,25,36–39]. However, to achieve this, we need, among others, (i) a meticulous treatment of the stellar matter with state-of-art nuclear theory EoSs to account for temperature and composition dynamics and (ii) an approach to incorporate microphysical processes such as neutrinos-driven reactions that related to nucleosynthesis. In particular, requirement (ii) is corroborated by the observed kilonova AT2017gfo, which suggests the importance of r -process nucleosynthesis [40,41] in neutron-star merger outflows.

In this work, we explain recent updates to the NR code BAM [42–45] focusing on the implementation of a Neutrino Leakage Scheme (NLS) [46,47] to describe neutrino production and transport using tabulated nuclear-theory based EoSs, and subsequent modifications to the General Relativistic Hydrodynamics (GRHD) routines. We validate our code extensions with a variety of tests and present a set of new BNS simulations.

The structure of this article is as follows. In Section 2 we discuss the underlying theory and summarize the basic equations that we modified in order to incorporate neutrino interactions. In Section 3 we outline the employed numerical methods and implementation. Tests for our new scheme, i.e., single TOV evolutions undergoing neutrino-induced collapse, are shown in Sec. 4. In Section 5 we present BNS simulations and we conclude in Sec. 6. Throughout this work we employ geometric units ($c = G = 1$), and we set Boltzmann constant and the mass of the sun equal to one, i.e., $M_\odot = k_B = 1$. The metric signature is $(-, +, +, +)$, Greek indices μ, ν, \dots run from 0-3 while Latin indices i, j, \dots run from 1-3, and Einstein's summation convention is employed.

2. Fundamental Equations

2.1. 3+1 Decomposition and Spacetime Evolution

BAM employs the 3+1 decomposition formalism, i.e., the 4-dimensional spacetime is foliated by a set of non-intersecting 3-dimensional spacelike hypersurfaces Σ , with a field of timelike normal vectors n^μ . The spacetime coordinates are chosen such that the line element reads

$$ds^2 = -\alpha^2 dt^2 + \gamma_{ij}(\beta^i dt + dx^i)(\beta^j dt + dx^j), \quad (1)$$

where $\alpha > 0$ is the lapse function, $\gamma_{\mu\nu} = g_{\mu\nu} + n_\mu n_\nu$ is the spatial metric induced on the hypersurfaces Σ , β^i is the spatial shift vector, and dx^i is the spatial coordinates displacement. Likewise, the components of the normal field are given by

$$n^\mu = (\alpha^{-1}, -\alpha^{-1}\beta^i), \quad (2)$$

$$n_\mu = (-\alpha, 0, 0, 0). \quad (3)$$

For the dynamical evolution of the spacetime, we are using the BSSNOK scheme ([48] and references therein) for the TOV runs, while for the BNS runs we make use of the Z4c scheme ([49] and references therein).¹

2.2. General Relativistic Radiative Hydrodynamics

The covariant GRHD equations arise from the relevant conservation laws. The first of which is the baryon number conservation

$$\nabla_\mu(\rho u^\mu) = 0, \quad (4)$$

where ∇_μ is the covariant derivative compatible with the spacetime metric $g_{\mu\nu}$, $\rho = m_b n_b$ is the rest-mass density, with m_b being a baryon mass constant chosen depending on the EoS and

¹ We note that this choice of evolution scheme is somewhat arbitrary.

n_b is the baryon number density; u^μ is the matter element four-velocity, that in terms of 3+1 fields is written as

$$u^\mu = W(n^\mu + v^\mu), \quad (5)$$

where v^μ is the spatial velocity measured by the Eulerian frame, $v^\mu n_\mu = 0$, $W = 1/\sqrt{1 - v^2}$ is the Lorentz factor and $v^2 = \gamma_{ij}v^i v^j$.

The second equation is the energy-momentum conservation, given by

$$\nabla_\nu T^{\mu\nu} = 0, \quad (6)$$

where $T_{\mu\nu}$ is the stress-energy tensor. Within this work, we describe matter as an ideal fluid, hence

$$T_{\text{fluid}}^{\mu\nu} = (e + p)u^\mu u^\nu + pg^{\mu\nu}, \quad (7)$$

where e is the energy density and p is the pressure measured in the fluid comoving frame. If the spacetime is filled with matter and neutrinos, the stress-energy tensor becomes

$$T^{\mu\nu} = T_{\text{fluid}}^{\mu\nu} + T_{\text{rad}}^{\mu\nu}, \quad (8)$$

where $T_{\text{rad}}^{\mu\nu}$ is the stress-energy tensor of the neutrinos, hereby modeled as radiation. Hence, Equation (6) reads

$$\nabla_\nu T_{\text{fluid}}^{\mu\nu} = -\nabla_\nu T_{\text{rad}}^{\mu\nu} \equiv \Psi^\mu, \quad (9)$$

where we defined for convenience $\Psi^\mu \equiv -\nabla_\nu T_{\text{rad}}^{\mu\nu}$. Equation (9) then states that energy and momentum are carried away by neutrinos, producing variations on the energy and momentum of a fluid element.

In addition, incorporating neutrino-driven reactions, the conservation of leptons must be enforced explicitly. Provided that the only lepton species in the fluid are electrons and positrons, the relevant conservation law reads

$$\nabla_\mu (\rho Y_e u^\mu) = \rho \mathcal{R}, \quad (10)$$

where $Y_e = n_e/n_b$ is the electron fraction, n_e is the net electron number density, and \mathcal{R} is a source term accounting for the variations of the lepton number within a matter element in response to the emission/absorption of neutrinos. In fact Equation (10) implies, with the help of Equation (4), that

$$u^\mu \nabla_\mu Y_e = \frac{dY_e}{d\tau} = \mathcal{R}, \quad (11)$$

where $d\tau$ is the proper time elapsed for a matter element. Hence, \mathcal{R} can be understood as the rate of change of the electron fraction measured in the fluid rest-frame.

The next step is to bring Equations (4), (9), (10), that constitute the GRHD equations in covariant formulation into the correspondent coordinate expressions as the following balance law

$$\partial_0 \mathbf{q} + \partial_i \mathbf{F}^i(\mathbf{q}) = \mathbf{S}(\mathbf{q}), \quad (12)$$

known as the Valencia formulation of the GRHD equations [50]. Equation (12) is a system of six partial differential equations that performs the time evolution of the *conserved* quantities

$$\mathbf{q} \equiv \sqrt{\gamma} \begin{pmatrix} D \\ \tau \\ S_k \\ DY_e \end{pmatrix} = \sqrt{\gamma} \begin{pmatrix} W\rho \\ \rho h W^2 - p - W\rho \\ \rho h W^2 v_k \\ \rho W Y_e \end{pmatrix}, \quad (13)$$

where γ is the determinant of the spatial metric, D is the rest-mass density, τ is the energy density, S_k is the momentum density and DY_e is the conserved electron fraction, all measured in the Eulerian frame, which are defined in terms of the *primitive* quantities

$$\mathbf{w} \equiv (\rho, \epsilon, v_k, p, Y_e), \quad (14)$$

where ϵ is the specific internal energy per baryon and $h = 1 + \epsilon + p/\rho$ is the specific enthalpy per baryon. The fluxes are

$$\mathbf{F}^i \equiv \sqrt{\gamma} \begin{pmatrix} D(\alpha v^i - \beta^i) \\ \tau(\alpha v^i - \beta^i) + \alpha p v^i \\ S_k(\alpha v^i - \beta^i) + \alpha p \delta^i_k \\ DY_e(\alpha v^i - \beta^i) \end{pmatrix}, \quad (15)$$

and the source terms read

$$\mathbf{S} \equiv \sqrt{\gamma} \begin{pmatrix} 0 \\ \alpha \mathcal{S}^{ij} K_{ij} - S^i \partial_i \alpha + \alpha^2 \Psi^0 \\ \frac{\alpha}{2} S^{ij} \partial_k \gamma_{ij} + S_i \partial_k \beta^i - (\tau + D) \partial_k \alpha + \alpha \Psi_k \\ \alpha \rho \mathcal{R} \end{pmatrix}, \quad (16)$$

with $\mathcal{S}_{ij} \equiv \gamma_{i\mu} \gamma_{j\nu} T_{\text{fluid}}^{\mu\nu}$ being the spatial stress tensor of the matter distribution.

In order to close the GRHD system of equations, an EoS must be provided to compute the pressure p from the remaining primitives. One of our new additions to the BAM code is related to this point. Instead of providing as input a 1-dimensional EoS $p_{\text{cold}}(\rho)$ parametrized as a piecewise polytrope [51] augmented with a Γ -law EoS to model thermal effects, i.e. $p = p_{\text{cold}} + p_{\text{th}}$ with $p_{\text{th}} = (\Gamma - 1)\rho\epsilon$ [52], we consider more general and realistic nuclear-theory EoSs in the form of 3-dimensional tables. In this scenario, the necessary thermodynamical quantities are represented as functions of the rest-mass density, temperature and electron fraction, and are computed via trilinear interpolations.

2.3. Neutrino Leakage

The NLS has been employed for a variety of astrophysical systems to model neutrino emission, e.g., Core-Collapse Supernovae [53–55] and compact binary mergers [46,47,56–59]. It possesses a number of advantages such as (i) a simple implementation, (ii) reasonable (qualitative) description of neutrinos features in NSs, particularly in optically thick media ([58] and references therein) and (iii) low computational costs. Therefore, its implementation in numerical-relativity simulations is compelling. Moreover, despite the underlying assumptions of the approach (that will become clear in the following), the NLS serves as a first approximation for radiative losses and is a basis to support more intricate and realistic methods, e.g., in radiation transport moment schemes [60–67], Lattice-Boltzmann methods [68], or advanced leakage schemes [69–71].

2.3.1. Underlying Hypotheses of the Neutrino Leakage Scheme

The NLS is characterized by a number of hypotheses or assumptions outlined in, e.g., Ref. [72]. For completeness, we will also describe the most important aspects in the following.

1. The only lepton species within the fluid are electrons and positrons.
2. The considered neutrino flavors are electron neutrinos ν_e , electron antineutrinos $\bar{\nu}_e$, and heavy leptons neutrinos/antineutrinos $\nu_{\mu,\tau}$, $\bar{\nu}_{\mu,\tau}$, collectively grouped as a single species ν_x with statistical weight 4.

3. Neutrinos obey the ultra-relativistic Fermi-Dirac distribution in local β -equilibrium and have the same temperature as the matter. Hence, the relativistic chemical potentials (i.e., including rest-masses of protons, neutrons, and electrons) for electron-flavored neutrinos read

$$\mu_{\nu_e} = -\mu_{\bar{\nu}_e} = \mu_p + \mu_e - \mu_n, \quad (17)$$

where, for simplicity, we assume $\mu_{\nu_x} = 0$ given that heavy lepton neutrinos rarely interact with matter.

4. The emission of neutrinos is isotropic in the fluid rest-frame and is given by

$$\Psi^\mu = -n_b \mathcal{Q} u^\mu, \quad (18)$$

where the total emissivity \mathcal{Q} (energy per unit time and baryon) is the sum of emissivities for all neutrino flavors

$$\mathcal{Q} \equiv \mathcal{Q}(\nu_e) + \mathcal{Q}(\bar{\nu}_e) + \mathcal{Q}(\nu_x). \quad (19)$$

To see that Equation (18) corresponds to an isotropic emission, note that the projection of Ψ^μ onto the hypersurface orthogonal to the fluid worldlines via the projector $h_{\mu\nu} = g_{\mu\nu} + u_\mu u_\nu$ vanishes, i.e., $h_{\mu\nu} \Psi^\mu = 0$. Hence, the neutrinos are emitted such that no net momentum flux is perceived in the fluid comoving frame.

5. The source term \mathcal{R} is given by

$$\mathcal{R} \equiv R(\bar{\nu}_e) - R(\nu_e), \quad (20)$$

i.e., the creation of electron (anti) neutrinos demand the (creation) annihilation of an (electron) positron in order to conserve the lepton family number.

6. Neutrinos are treated as a ‘test’ fluid. Hence, the projections of $T_{\text{rad}}^{\mu\nu}$, that act as sources of spacetime curvature, are neglected.

Furthermore, the pressure and specific internal energy of a volume containing matter and neutrinos is given by

$$p = p_{\text{fluid}} + p_{\nu_e} + p_{\bar{\nu}_e} + p_{\nu_x}, \quad \epsilon = \epsilon_{\text{fluid}} + \epsilon_{\nu_e} + \epsilon_{\bar{\nu}_e} + \epsilon_{\nu_x}. \quad (21)$$

Nevertheless, the neutrino contributions to the above equations are only reasonable in opaque media (in which the neutrinos are said to be *trapped*), where radiation mostly diffuses in equilibrium with its surroundings. In semi-transparent media, where neutrinos rarely interact with the matter, radiation flows as *freely streaming*, hence no pressure is exerted by neutrinos nor energy transfer occurs between matter and radiation. Besides, the spatial identification of trapped, freely streaming and ‘gray’ regimes within a NS is hardly feasible beforehand and it is very difficult to capture and encode them in Equations (21), at least in a NLS framework. Therefore we opt for a simpler approach in which the pressure and specific internal energy contributions of neutrinos are neglected within the whole extent of a NS. It is straightforward to verify that if neutrinos are described by an ultra-relativistic Fermi-Dirac distribution, their pressure and specific internal energy contributions are only sizeable in low-density, high temperature regions, where interactions rarely occur. Thus, the error made in the approximation $p \approx p_{\text{fluid}}$, $\epsilon \approx \epsilon_{\text{fluid}}$ is negligible.

It is worth pointing out that the adoption of the ‘test’ fluid hypothesis only simplifies our treatment of neutrinos with respect to their *direct* role in the spacetime and matter evolutions. Thus, what remains is the way in which neutrinos alter the hydrodynamics [as of Equations (22)-(24) below].

We end this section by explicitly showing how the previously introduced GRHD equations have to be modified following the previous hypotheses. While the baryon number conservation

remains unaltered, the energy density, momentum density and conserved electron fraction evolve, respectively, according to

$$\partial_0(\sqrt{\gamma}\tau) + \partial_i[\sqrt{\gamma}\tau(\alpha v^i - \beta^i) + \sqrt{\gamma}\alpha p v^i] = \sqrt{\gamma}(\alpha \mathcal{S}^{ij}K_{ij} - S^i\partial_i\alpha) - \alpha\sqrt{\gamma}\mathcal{Q}m_b^{-1}D, \quad (22)$$

$$\begin{aligned} \partial_0(\sqrt{\gamma}S_k) + \partial_i[\sqrt{\gamma}S_k(\alpha v^i - \beta^i) + \sqrt{\gamma}\alpha p \delta^i_k] &= \sqrt{\gamma}\left(\frac{\alpha}{2}\mathcal{S}^{ij}\partial_k\gamma_{ij} + S_i\partial_k\beta^i - (\tau + D)\partial_k\alpha\right) \\ &\quad - \alpha\sqrt{\gamma}\mathcal{Q}m_b^{-1}Dv_k, \end{aligned} \quad (23)$$

$$\partial_0(\sqrt{\gamma}DY_e) + \partial_i[\sqrt{\gamma}DY_e(\alpha v^i - \beta^i)] = \alpha\sqrt{\gamma}\mathcal{R}\frac{D}{W}. \quad (24)$$

The additional terms due to the NLS are marked in red.

2.4. Emissivities and Production Rates

The classification of radiative regimes within a NS suggests a natural division between free and diffusive processes. In our scheme, the free emission rates account for the most potent reactions, including:

(i) Direct Urca process, comprised of positron capture by neutrons

$$e^+ + n \rightarrow p + \bar{\nu}_e, \quad (25)$$

and electrons capture by protons

$$e^- + p \rightarrow n + \nu_e. \quad (26)$$

(ii) Electron-positron-pair annihilation

$$e^- + e^+ \rightarrow \nu_e + \bar{\nu}_e, \quad e^- + e^+ \rightarrow \nu_\mu + \bar{\nu}_\mu, \quad e^- + e^+ \rightarrow \nu_\tau + \bar{\nu}_\tau. \quad (27)$$

(iii) Transversal plasmon decay

$$\gamma \rightarrow \nu_e + \bar{\nu}_e, \quad \gamma \rightarrow \nu_\mu + \bar{\nu}_\mu, \quad \gamma \rightarrow \nu_\tau + \bar{\nu}_\tau. \quad (28)$$

The expressions employed to estimate emissivities and production rates of the above processes can be found in Ref. [46]. The free emissivity rate $Q^F(I)$ and the free production rate $R^F(I)$ (with $I = \nu_e, \bar{\nu}_e, \nu_x$) are the sum of emission rates over the reactions r , i.e.,

$$Q^F(I) = \sum_r Q_r(I), \quad R^F(I) = \sum_r R_r(I). \quad (29)$$

The diffusive processes are:

(i) Neutrino-elastic scattering on a representative heavy nucleus X and atomic mass number A .

$$\nu_e + A \rightarrow \nu_e + A, \quad \bar{\nu}_e + A \rightarrow \bar{\nu}_e + A, \quad \nu_x + A \rightarrow \nu_x + A. \quad (30)$$

(ii) Neutrino-elastic scattering on free nucleons

$$\nu_e + [n, p] \rightarrow \nu_e + [n, p], \quad \bar{\nu}_e + [n, p] \rightarrow \bar{\nu}_e + [n, p], \quad \nu_x + [n, p] \rightarrow \nu_x + [n, p]. \quad (31)$$

(iii) Electron-flavor neutrino absorption on free nucleons

$$\nu_e + n \rightarrow p + e^-, \quad \bar{\nu}_e + p \rightarrow n + e^+. \quad (32)$$

The I neutrinos mean free path λ_I , which is a function of the neutrinos energy E_I , is defined as

$$\lambda_I^{-1} \equiv n_p[\sigma_{I,s}(p) + \sigma_{I,a}(p)] + n_n[\sigma_{I,s}(n) + \sigma_{I,a}(n)] + n_h\sigma_{I,s}(X), \quad (33)$$

where n_p , n_n , n_h are the protons, neutrons, and heavy nuclei number densities, respectively. The neutrino energy dependency is introduced by the scattering (subscript s) and absorption (subscript a) cross sections found in Ref. [46]. In order to classify how opaque is a medium with respect to I neutrino, the optical depth is defined as

$$\tau_I(E_I) \equiv \int_{s_1}^{s_2} \frac{ds}{\lambda_I(E_I)}, \quad (34)$$

where the above line integral is evaluated along the invariant line element from Equation (1) with $dt = 0$ parametrized by s between s_1 and s_2 . Since all cross sections used in this work depend on E_I^2 , it is useful to factor them out in the form $\zeta_I = (E_I^2 \lambda_I)^{-1}$ and to define the energy-independent optical depth as

$$\chi_I \equiv \int_{s_1}^{s_2} \zeta_I ds, \quad (35)$$

where a discussion of the method adopted to estimate χ_I is presented in Sec. 3.2. Finally, in terms of χ_I Equation (34) reads

$$\tau_I = E_I^2 \chi_I. \quad (36)$$

If E_I^2 is taken to be the ultra-relativistic Fermi-Dirac ensemble average, the expression above becomes

$$\tau_I = \chi_I \frac{F_4(\eta_I)}{F_2(\eta_I)} T^2, \quad (37)$$

for the degeneracy parameters $\eta_I = \mu_I/T$. In our implementation the incomplete Fermi-Dirac integrals

$$F_k(\eta) = \int_0^\infty \frac{x^k dx}{\exp(x - \eta) + 1}, \quad (38)$$

are computed by the analytic fittings of Ref. [73]. The *neutrinosphere* of the I 'th neutrino is defined as the surface at which $\tau_I = 2/3$ and serves the purpose of dividing the optically thick region ($\tau_I > 2/3$), where diffusive processes dominate, from the optically thin region ($\tau_I < 2/3$), where free emission processes are more important.

Although emissivities and production rates may be estimated for diffusive and freely streaming regimes, the optical properties of NS matter with respect to neutrinos may lie in an intermediate regime. Therefore, to capture this feature, we employ effective emissivities $Q_{\text{eff}}(I)$ and effective production rates $R_{\text{eff}}(I)$ at each point defined by the interpolation [47,57,72]

$$Q_{\text{eff}}(I) \equiv Q(I) = \frac{Q^F(I)Q^D(I)}{Q^F(I) + Q^D(I)}, \quad R_{\text{eff}}(I) \equiv R(I) = \frac{R^F(I)R^D(I)}{R^F(I) + R^D(I)}, \quad (39)$$

where the diffusive emissivity $Q^D(I)$ and the diffusive production rate $R^D(I)$ are given by [47]

$$Q^D(I) = \frac{4\pi g_I}{(hc)^3} \frac{\zeta_I}{3\chi_I^2} T^2 F_1(\eta_I), \quad R^D(I) = \frac{4\pi g_I}{(hc)^3} \frac{\zeta_I}{3\chi_I^2} T F_0(\eta_I), \quad (40)$$

with $g_{\nu_e} = g_{\bar{\nu}_e} = 1$, $g_{\nu_x} = 4$, and h being the Planck constant. $Q^F(I)$ and $R^F(I)$ are given by Equations (29). Then, Equations (39) are used to compute the NLS contributions to the GRHD source terms from Equations (19) and (20).

Finally, we estimate the source luminosity (i.e., not including redshift) for the I 'th neutrino species with the following expression [72]

$$L_I = \int d^3x \left[\alpha \sqrt{\gamma} W n_b Q(I) \frac{(\alpha - \beta^i v_i)}{\sqrt{-g_{00}}} \right], \quad (41)$$

which comes from integrating the energy per unit time measured by a coordinate observer over a refinement level.

3. Numerical Implementation

BAM uses a hierarchy of L nested Cartesian levels labeled with $l = 0, 1, \dots, L - 1$. The moving levels $l \geq l_{\text{mv}}$ contain n_{mv} points per direction and can move to track the motion of the stars, while the static levels $l < l_{\text{mv}}$ contain n points per direction and are fixed. The constant distance between grid points within one level is given by $h_l = h_0/2^l$, where h_0 is the distance between grid points in level 0. The fluxes in the GRHD Equations (12) are estimated employing a High Resolution Shock-Capturing scheme based on primitives reconstruction at cell interfaces using the WENOZ scheme [74], the Local Lax-Friedrichs (LLF) approximate Riemann solver [75] and a conservative mesh refinement strategy. The time evolution is performed adopting the Method of Lines and a 4th-order Runge-Kutta integrator.

3.1. Code Updates

1. In our previous studies using the BAM code, we used mainly one-parameter piecewise polytropes EoSs together with an ideal-gas thermal contribution. Now, we have extended this infrastructure to enable the use of three-dimensional tables. In general, these tables have a finite range of validity defined as a domain \mathcal{D} with

$$\mathcal{D} = \{(\rho, T, Y_e) : \rho_{\min} \leq \rho \leq \rho_{\max}, T_{\min} \leq T \leq T_{\max}, Y_{\min} \leq Y \leq Y_{\max}\}. \quad (42)$$

For this purpose, EoS evaluations should only be performed within this domain, i.e., additional checks have to be incorporated into BAM.

2. Previously adopted EoSs allowed us to use a simple and fast converging root-finding procedure for the conservative-to-primitive conversion. This is not the case for a three-parameter tabulated EoS, since numerical derivatives computed by trilinear interpolations are noisy. In our case, we use the methods outlined in Refs. [72,76] to ensure a robust conservative-to-primitive conversion.

3. Once we employ three-parameter EoSs, we also have to solve Equation (24).

4. We make use of a static and cold atmosphere to model vacuum, i.e., grid points with $\rho \leq \rho_{\text{fac}} \times \rho_{\text{atm}}$ (here we use $\rho_{\text{fac}} = 10$ and $\rho_{\text{atm}} = 10 \times \rho_{\min}$) are set to

$$\rho = \rho_{\text{atm}}, \quad v^i = 0, \quad T = T_{\min} = 0.1 \text{ MeV}, \quad Y = Y_{\text{atm}}.$$

We use $Y_{\text{atm}} = 0.4$ in our TOV simulations in order to reproduce conditions of testbeds reported in the literature and $Y_{\text{atm}} = Y_{\min} = 0.01$ in our BNS runs so that the pressure of the atmosphere $p_{\text{atm}} = p(\rho_{\text{atm}}, T_{\text{atm}}, Y_{\text{atm}})$ is lowest.

3.2. Free Emission Rates and Optical Depth Estimates

Using the β -equilibrium condition, Equation (17), and the local thermal equilibrium hypothesis allows us to compute the free emission rates $R^F(I)$, $Q^F(I)$ for the processes outlined in Equations (25)-(28) directly from the EoS. During the code initialization, we build auxiliary tables for the emission rates and ζ_I , then any required value along the simulation is computed by trilinear interpolation of the tables. Next, in order to calculate the effective emission rates, the

Table 1. Properties of the TOV stars. From left to right the columns read: model name, central rest-mass density, gravitational mass, baryonic mass, emitted neutrino energy (up to the collapse for those evolved with NLS), grid resolution and distance between grid points on the finest level. The central densities for this test were chosen to meet the same initial conditions of Ref. [72]. The top row ‘Maximal’ refers to the model on the onset of instability.

Model	$\rho_c [10^{15} \text{ g/cm}^3]$	$M [M_\odot]$	$M_b [M_\odot]$	$E [10^{51} \text{ erg}]$	n	$h_2 [\text{m}]$
Maximal	1.068	2.797	3.506	-	-	-
A	1.079	2.798	3.310	2.045	256	111
B	1.111	2.796	3.309	1.232	192	148
C	1.218	2.784	3.293	0.712	128	207

diffusive emission rates $R^D(I)$, $Q^D(I)$ also have to be computed, which requires determining the energy-independent optical depth χ_I of Equation (40). Due to the lack of knowledge about the trajectory of the neutrinos within a material medium, we resort to Fermat’s principle in order to choose the energy-independent optical depth, Equation (35), at each grid point k as the minimum χ_I among the six first neighbors along the $d(=x, y, z)$ coordinate directions, i.e.,

$$\chi_{I,k} = \min \left[\bar{\zeta}_{I,d}^\pm \sqrt{\bar{\gamma}_{dd}^\pm} \Delta x_d \right], \quad (43)$$

where $\bar{\zeta}_{I,d}^\pm$ ($\bar{\gamma}_{dd}^\pm$) is the average ζ_I (γ_{dd}) between the point k and the neighbors at $\pm d$ directions. Δx_d is the grid spacing in the d direction.

It is worth pointing out that although more elaborate approaches for the energy-independent optical depth estimation are possible, e.g. ray-by-ray integrating up to the boundaries of the computational domain [56], using an auxiliary grid adapted to the symmetry of the system [72] or iteratively over the entire grid [57,59], such prescriptions tend to further increase computational costs and often violate special relativity.

4. Neutrino-induced collapse of single TOV stars

Our first aim is it to test our implementations by reproducing the neutrino-induced gravitational collapse reported in Ref. [72]. We employ the SHT-NL3 EoS [77] initially in neutrino-less β -equilibrium at constant $T = 30 \text{ MeV}$. Integrating the TOV equations [78] for various central rest-mass densities results in the mass-radius and mass-central rest-mass density curves depicted in Figure 1. For our simulations we consider three radially-unstable (according to the *turning point criterion* [79]) configurations identified by A, B, and C, with increasing rest-mass density from A to C. We evolve them with and without the NLS in a static three levels grid where the finest level encompasses the entire star. A summary of the setups is found in Table 1.

There are two main differences between our implementation and that of Ref. [72]. First, we employ the fifth-order WENOZ reconstruction [74] instead of the third-order piecewise parabolic method [80]. Thus, our reconstruction method is subject to less numerical viscosity. Second, we estimate opacities (and hence diffusive rates) by integrating the mean free paths along the x , y , z coordinate directions up to neighboring points.

In Figure 2, we present the central rest-mass density evolution for simulations without NLS (A, B, C) on the left panel and with NLS (A- ν , B- ν , C- ν) on the right panel. During the simulations the stars without NLS evolve stably, while NLS simulations show the characteristic density growth and gravitational collapse. The gravitational collapse is caused by the cooling and deleptonization that occurs more intensely in medium-low density regions of the star

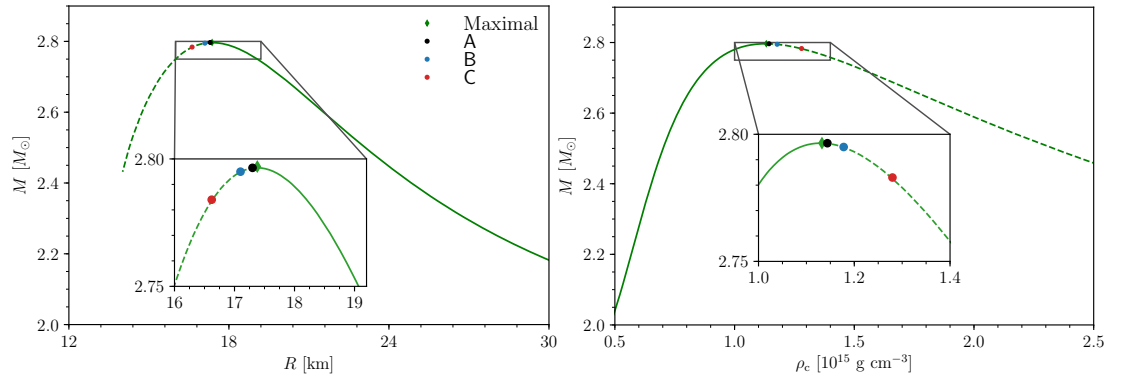


Figure 1. TOV solutions for the SHT-NL3 EoS in neutrino-less β -equilibrium and constant $T = 30$ MeV. The marked points refer to the configurations of Table 1: Maximal (green diamond), A (black circle), B (blue circle), and C (red circle). *Left panel:* Mass-radius curve. *Right panel:* Mass-central rest-mass density curve. The solid line represents the stable branch, while the dashed line represents the unstable branch.

and leads to the decrease of the pressure exerted by those fluid elements. Unable to resist the gravitational attraction, the outer envelopes are pulled towards the dense core, decreasing the star radius and increasing the central rest-mass density. In the cases shown, the additional pressure due to the denser configuration was not enough to prevent the collapse. In the cases with NLS, the oscillatory evolution of the rest-mass density follows from the coupling between the fluid motion and the emission of neutrinos, which are responsible for carrying away energy-momentum from the matter. Overall, the collapse takes place sooner for higher central rest-mass density since the NS is more unstable to radial oscillations, which also explains the ordering of the observed collapse time in Figure 2.

In the lower panel of Figure 2 we present the total neutrino luminosity during the simulations with NLS, where an initial burst of neutrinos is apparent due to the high initial temperature and the abundance of nucleons and electrons powering very energetic neutrino-driven reactions in semi-transparent regions of the star. The luminosity fades over time as a consequence of the rapid cooling of medium-low density material until it dips when an event horizon is formed.

The temperature profile evolution for runs A and A- ν are presented in Figure 3 at $t = (0.00, 1.08, 8.54)$ ms, which corresponds, respectively, to the initial configuration, the end of the first expansion cycle and the onset of the apparent horizon detection. We observe that the ν_e -neutrinosphere recedes towards the core. The outside (optically thin) regions are found effectively cooled, while inside the neutrinosphere the dominance of diffusive processes prevents the temperature loss. On the onset of gravitational collapse ($t = 8.54$ ms) the internal layers are heated by compression.²

In Figure 4 we present snapshots of the electron neutrinos emissivity and the electron fraction for the longer-lived run A- ν . We see that in the low density envelope (with rest-mass densities between the atmosphere value $\rho_{\text{atm}} = 10^7 \text{ g cm}^{-3}$ and $\rho = 10^{12} \text{ g cm}^{-3}$) the emissivity decreases more than three orders of magnitude and the matter strongly deleptonizes [from $t = 0$ ms (left panel) to $t = 1.08$ ms (central panel)]. This occurs within the first expansion cycle of the star and explains the early burst in the bottom panel of Figure 2. In the middle panels, the formation of eddies on a circle with radius $r = \sqrt{x^2 + y^2} \sim 10$ km is related to

² It is important to mention that in order to reproduce the neutrinos-induced collapse we need to employ finer grids for TOV stars near the maximal ρ_c (see Table 1). This is because at higher resolutions we find smaller mean free paths among the coordinate directions, which lead to higher effective emission rates and to a sufficient cooling of the matter to trigger the collapse.

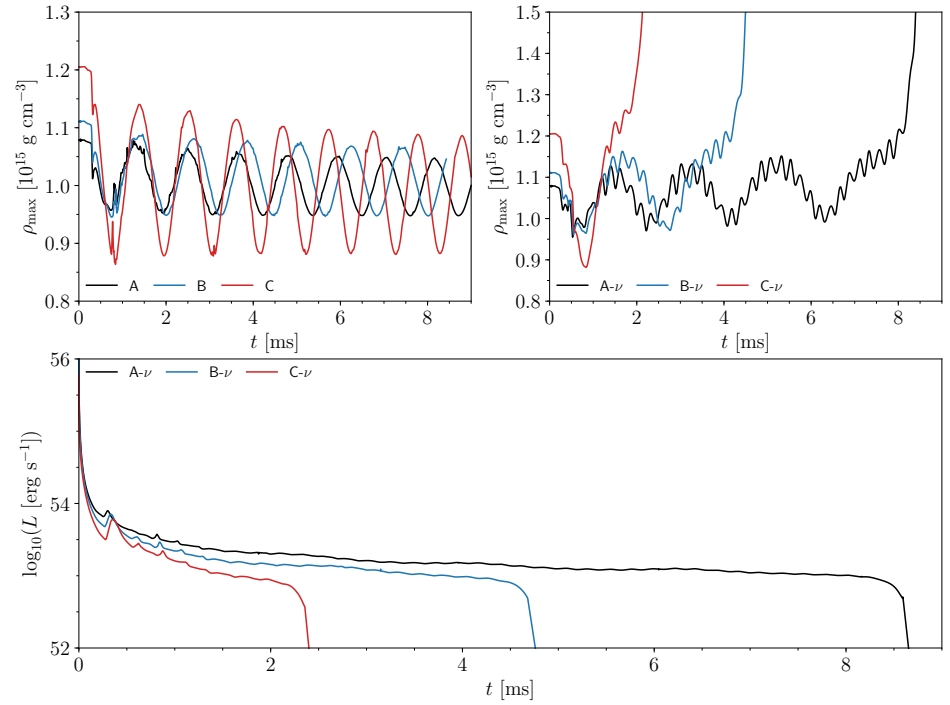


Figure 2. Time evolution of quantities of interest. *Upper panels:* central rest-mass density for simulations A, B and C. *Left panel:* without NLS, where the density evolves stably around an equilibrium state for each run. *Right panel:* with NLS, where the wobbly evolution results from the coupling between the matter motion and the neutrinos emission. A final density growth marks the formation of an event horizon. *Lower panel:* Total luminosity evolution for simulations A- ν , B- ν and C- ν . We notice a rapid burst at the beginning of the simulations. Likewise, the oscillating pattern of the luminosity is a consequence of the coupling between neutrinos and matter. After the formation of the event horizon, the luminosity abruptly decreases.

convective instabilities as predicted by the Ledoux criterion [81]. On the right panels the star is on the verge of gravitational collapse. Note that along the evolution, the emissivity and electron fraction is almost unaltered within the $\rho \geq 10^{14}$ g/cm³ opaque region because much less energetic diffusive processes dominate the emissions.

5. BNS Simulations

In order to compare the performance of our implementations in the case of BNSs with those reported in the literature, in particular Ref. [58], we first performed short inspiral (~ 2 to 4 orbits), single resolution simulations for equal-mass, non-spinning BNSs described by the SFHo [82] and the DD2 [83] EoSs, with and without our NLS implementation. Both EoSs contain neutrons, protons, electrons and positrons, initially at constant $T = 0.1$ MeV and in β -equilibrium. Besides the goal of comparing results, DD2 is a stiff EoS and SFHo is a soft EoS, hence, it is useful to assess our code capability to handle NSs belonging to both higher and lower compactness.

Furthermore, in order to evaluate the accuracy of our code, we performed long inspiral simulations (~ 14 orbits) using the BHB $\Lambda\phi$ EoS [84] (which contains protons, neutrons, electrons, positrons, the Λ_0 hyperon and the ϕ meson) with four different grid resolutions, with and without our NLS implementation. We choose this EoS to test our code with a microphysical description that contains a transition between pure nucleonic matter to hyperonic matter at high densities, thus representing a notably distinct scenario than that addressed by DD2

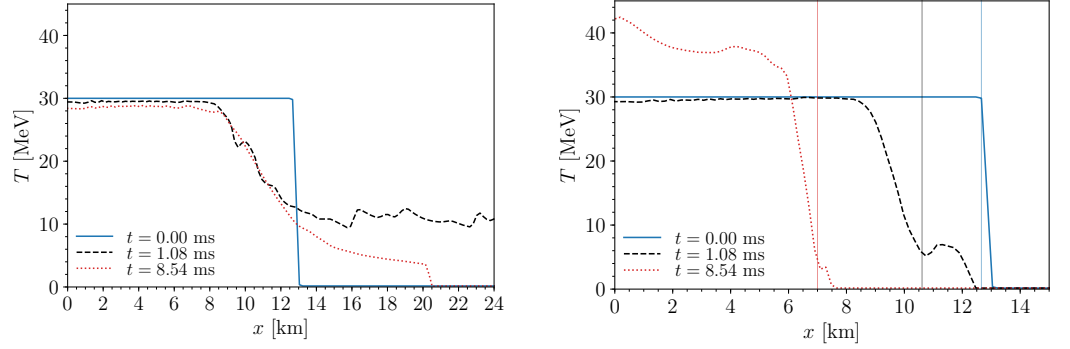


Figure 3. Temperature profile evolution inside the star along the coordinate x direction at the innermost level $l = 2$. *Run A (Left panel):* We present temperatures up to the level $l = 2$ boundary to show that in this case the NS achieves stability by increasing its radius with respect to $t = 0$. We note that at $t = 1.08$ ms the NS is still expanding, while a stable configuration is found at $t = 8.54$ ms. *Run A- ν (Right panel):* The vertical lines mark the position of the electron neutrino neutrinosphere. In general, outside the neutrinosphere the material has lower temperatures and the cooling becomes less effective towards the core due to the dominance of diffusive processes. By the end of the first expansion cycle ($\sim t = 1.08$ ms) the internal temperatures are nearly unaltered, while a large portion outside the neutrinosphere is cooler. Likewise, on the verge of the gravitational collapse ($t = 8.54$ ms), the layers outside of the neutrinosphere are cold while the interior is hotter due to compression.

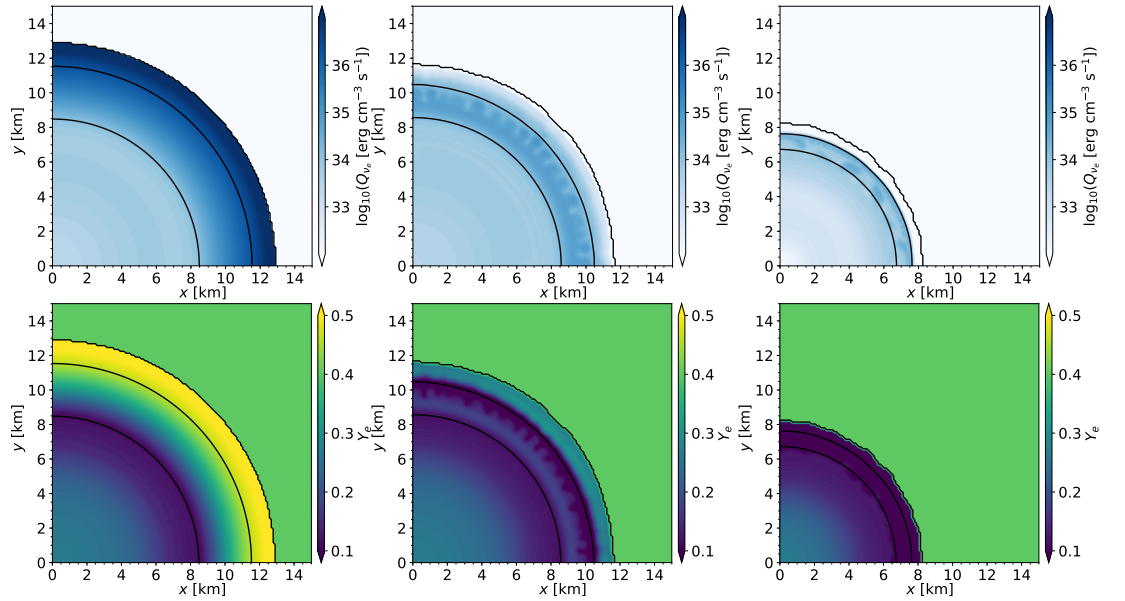


Figure 4. Snapshots of the A- ν simulation at $t = (0.00, 1.08, 8.64)$ ms from left to right. *Upper panels:* logarithm of the electron neutrinos emissivity. *Lower panels:* electron fraction. The solid black lines are contours of constant rest-mass density with $\log_{10}(\rho [\text{g cm}^{-3}]) = 7, 12, 14$. The outermost line marks the interface between the star and the atmosphere.

and SFHo. We consider the case of an equal-mass, non-spinning BNS system starting with a β -equilibrated, isentropic configuration with entropy per baryon $s \sim 1 = k_B$. All the EoS tables used in this work were obtained in the CompOSE online repository [85,86].

The grids used in all simulations have $L = 7$ refinement levels and the number of moving levels is set to $l_{mv} = 4$. Relevant information about grid and matter setups of our runs without

Table 2. Binary neutron star simulations. From left to right the columns read: simulation name, gravitational mass of the stars (A , B) in isolation, baryonic mass of the stars, compactness of the stars, tidal deformability of stars, ADM mass and ADM angular momentum of the BNS at the beginning of the simulation, initial coordinate distance between the stars, number of points per direction on the static levels, number of points per direction on the moving levels and grid spacing at the finest level.

Model	$M^{A,B} [M_\odot]$	$M_b^{A,B} [M_\odot]$	$C^{A,B}$	$\Lambda^{A,B} [\times 10^3]$	$M_{\text{ADM}} [M_\odot]$	$J_{\text{ADM}} [M_\odot^2]$	$d_0 [\text{km}]$	n	n_{mv}	$h_6 [\text{km}]$
DD2	1.200	1.292	0.134	1.616	2.375	5.612	36.2	256	128	0.199
SFHo	1.200	1.300	0.148	0.860	2.376	5.673	38.0	256	128	0.186
BHBA ϕ – R1	1.350	1.458	0.144	0.944	2.679	8.021	58.8	128	64	0.417
BHBA ϕ – R2	1.350	1.458	0.144	0.944	2.679	8.021	58.8	192	96	0.278
BHBA ϕ – R3	1.350	1.458	0.144	0.944	2.679	8.021	58.8	256	128	0.209
BHBA ϕ – R4	1.350	1.458	0.144	0.944	2.679	8.021	58.8	320	160	0.167

the NLS are found in Table 2. We identify the results of the NLS runs by appending the suffix $-\nu$ to the simulation name. In Appendix G we present a resolution study for the BHBA ϕ setup.

5.1. Initial Data

The initial data for our simulations were constructed using the pseudospectral SGRID code [87–90], which solves the 3+1 Constraint Equations in the conformal thin-sandwich approach [91–93] adopting a surface-fitting strategy. When this project started, SGRID only supported 1-dimensional piecewise polytropic (pwp) EoSs. Therefore, we reduce the 3-dimensional EoS to one dimension by imposing (i) neutrino-less β -equilibrium and (ii) either constant temperature or constant entropy per baryon s . Then, we parametrize the resulting 1-dimensional table as a pwp adopting a similar procedure as that of Ref. [51]. In order to validate our approach, we point out that the TOV solutions obtained with the 1-dimensional tables and the corresponding pwps have maximum differences in coordinate radii of $\sim 0.08\%$ and in the tidal deformabilities [94] of $\sim 1.2\%$ for our cases. For the longer runs, using the BHBA ϕ EoS, an eccentricity reduction procedure was employed [95].

5.2. Short Inspiral Simulations

In order to test our code and compare results with those of Ref. [58], we performed short inspiral simulations using the DD2, DD2- ν , SFHo and SFHo- ν focusing on the (2,2) mode of the GW and features of the post-merger stage, where the larger differences between the different cases appear. The inspiral stage in the SFHo and SFHo- ν simulations is composed of ≈ 4 orbits and took $t_{\text{mrg}} \approx 10.3$ ms to merge, while the DD2 and DD2- ν simulations are composed of ≈ 2 orbits and took $t_{\text{mrg}} \approx 6.2$ ms to merge. We consider the merger time as the time at which the amplitude of the (2,2) mode of the GW has its maximum.

5.2.1. Post-Merger Stage

In Figure 5 we present the maximum rest-mass density evolution during the post-merger phase of our simulations. The DD2 and SFHo cases agree with those reported in Ref. [58] and little difference is introduced by the adoption of the NLS. The softer SFHo undergoes a merger marked by an abrupt variation of the rest-mass density around $t - t_{\text{mrg}} = 0$ and a considerable increment over the whole remnant evolution. The stiffer DD2 case also exhibits these features but in a mildly way. Furthermore, in the figure we present the BHBA ϕ EoS which is an intermediate EoS located between the soft SFHo and the stiff DD2. This last mentioned EoS will be discussed in Section 5.3.

In Figure 6, we show the rest-mass density, temperature and electron fraction for the DD2 and SFHo EoSs (with and without the NLS) at 10 ms after the merger. Similar to the results of Ref. [58], we notice the formation of bar structures (the ‘smeared out’ $\rho \geq 10^{13} \text{ g cm}^{-3}$ region

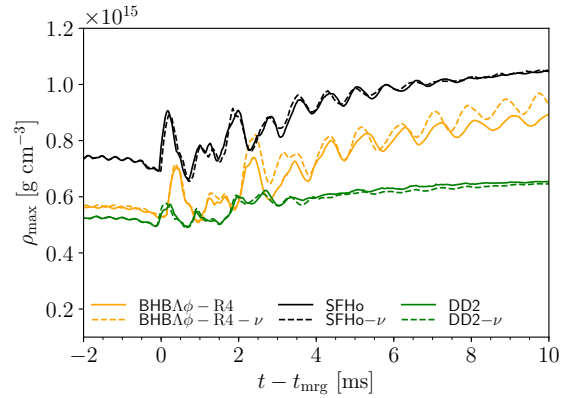


Figure 5. Post-merger evolution of the maximum rest-mass density ρ_{\max} reached by the different EoS considered in this article. Solid lines refer to the runs without NLS, while dashed lines represent the NLS runs. Our results for the SFHo and DD2 cases are in agreement with that reported in Ref. [58]. For the BHB $\Lambda\phi$ EoS we use resolution R4, see Table 2.

and the extended $\rho \lesssim 10^{13} \text{ g cm}^{-3}$ arms on the top panels), surrounded by dense disks. The difference in compactness is also visible, since DD2 develops a less dense core than SFHo and its disk extends further. Likewise, in the middle panels, hot interfaces between the colder bar and the disk are formed, with larger maximum temperatures reached by the softer SFHo EoS. Overall, the rest-mass density and temperature are less affected by the adoption of the NLS. A noticeable difference, however, is present on the electron fraction of the remnant (bottom panels), where the outer regions of the disk become neutron-rich while the core and arms are more leptonized. We were not able to reproduce the $Y_e \sim 0.2, 0.3$ of Ref. [58] at outer regions of the disk, which may be attributed to a key difference in our NLS implementation (see Ref. [57] for details): our optical depths are estimated from the minimum among first neighbors [as of Equation (43)] instead of integrating from the current position up to a computational domain boundary along minimum optical paths. This leads to smaller optical depths in our simulations and stronger deleptonization of the disk.

5.2.2. Spectrograms

In Figure 7, the spectrograms of the GWs of the DD2- ν and SFHo- ν runs (see Ref. [96] for details on the computation of the spectrograms) are presented in order to compare features of the post-merger GW signals with those reported in Ref. [58]. Our results are presented with respect to the retarded time u , given by

$$u = t - r_{\text{ext}} - 2M \ln(r_{\text{ext}}/2M - 1),$$

where we choose $r_{\text{ext}} = 600 M_{\odot}$ and $M = M^A + M^B$ is the total gravitational mass of the system. As expected, we find that the NLS has little effect on the emitted GW signals, as can be seen in the similarity between the filled red contours (NLS simulations) and gray contour lines (simulations without NLS) of Figure 7.

The SFHo spectrogram reproduces the same features as the one presented in Ref. [58]. Among them are, the strongest peak during post-merger which is clearly visible at frequency 2.95 kHz, a frequency gap between $\approx [2.0, 2.7]$ kHz. In relation with the DD2 spectrogram, it also reproduces the global features, with a gap between $\approx [2.0, 2.2]$ kHz and a stronger peak at ≈ 2.4 kHz.

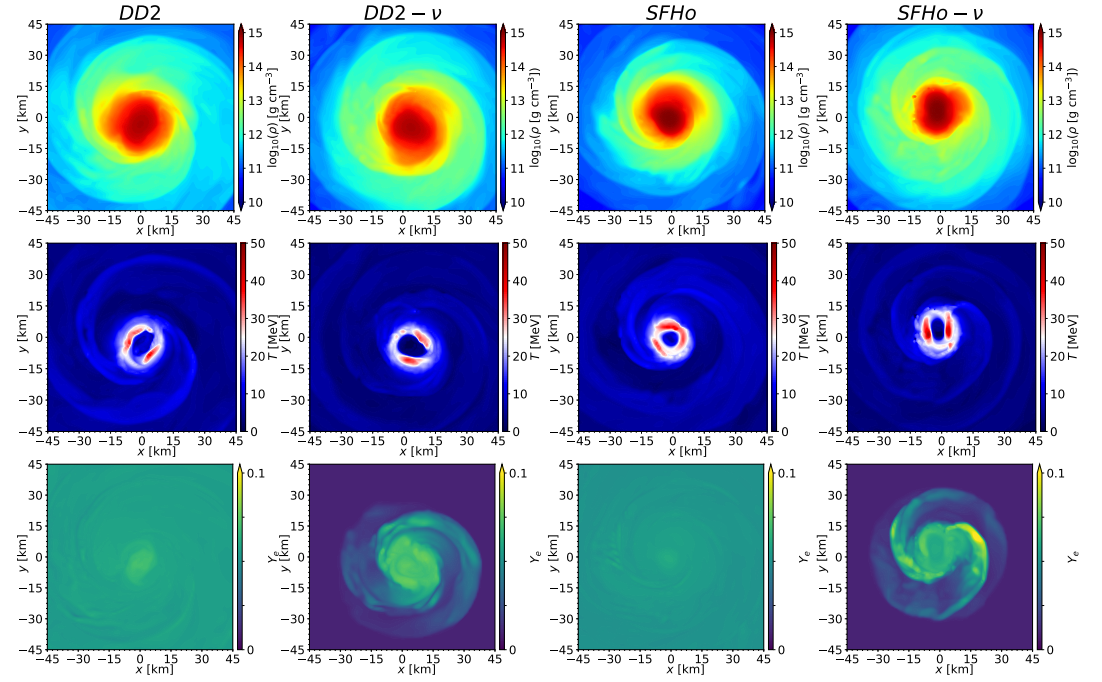


Figure 6. Snapshots of the remnant 10 ms after the merger in the $x - y$ plane. From left to right: DD2, DD2- ν , SFHo, and SFHo- ν . From top to bottom: rest-mass density, temperature and electron fraction. Overall we note the formation of bar-like structures (see the extended $\rho \geq 10^{13} \text{ g cm}^{-3}$ central regions and the $\rho \geq 10^{12} \text{ g cm}^{-3}$ arms in the top panels) surrounded by dense disks. The temperature profiles exhibit a hot interface between the bar and the disk. Finally, the effects of the NLS are perceivable on the electron fraction, where the disk becomes more neutron-rich as opposed to the cores and spiral arms.

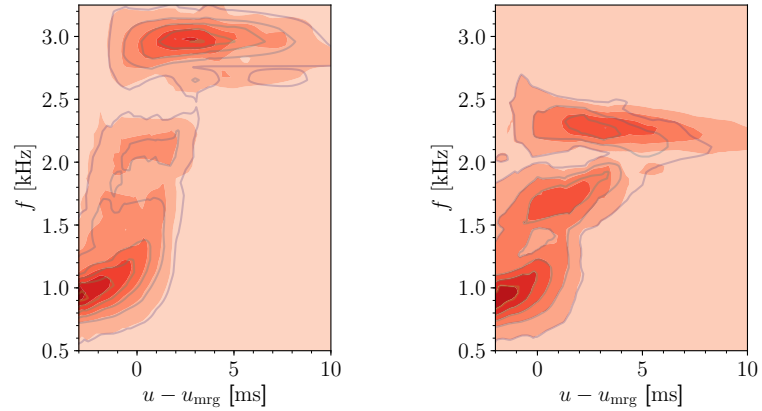


Figure 7. Spectrograms of the GWs for optimally oriented binaries and extracted at $r_{\text{ext}} = 600 M_{\odot}$. The contour lines represent the simulations without NLS. *Left panel:* SFHo- ν simulation, where the dominant post-merger frequency is 2.95 kHz. *Right panel:* DD2- ν simulation, where post-merger peak frequency is ≈ 2.4 kHz. Both panels share the same properties presented in Ref. [58].

5.2.3. Neutrinos Emission

As depicted in Figure 8, we see that the source luminosities, Equation (41), are negligible during the inspiral stage and increase towards the merger, when the compression of matter elements lead to an increase on the temperature. In both panels, we observe peaks for the three species around 2 to 3 ms after the merger, with the electron antineutrinos dominating up to

$t - t_{\text{mrg}} \sim 5$ ms, and then an overall decrease towards the end of the simulation. This behavior is consistent with Ref. [58], which then states that at $t - t_{\text{mrg}} = 10$ ms, $L_{\bar{\nu}_e} \sim (2 - 3) \times 10^{53} \text{ erg s}^{-1}$, with $L_{\bar{\nu}_e}$ dominating L_{ν_e} by a factor of 1.4 – 2. In our case, the electron antineutrinos luminosity lies within the same range and dominates the electron neutrinos luminosity by a factor of 1.7 – 2.3. Such an agreement is as good as we could expect for a leakage scheme. Concerning the total luminosity $L_{\text{tot}} = L_{\nu_e} + L_{\bar{\nu}_e} + L_{\nu_x}$, we find systematically higher values at the peaks than that reported in Ref. [58]. By the end of our simulations, we have $L_{\text{tot}} = 6.9 \times 10^{53} \text{ erg s}^{-1}$ for our SFHo run, which deviates less than 1% with respect to the counterpart of Ref. [58] and $L_{\text{tot}} = 5.8 \times 10^{53} \text{ erg s}^{-1}$ for the DD2 run, with a larger deviation of $\sim 20\%$.

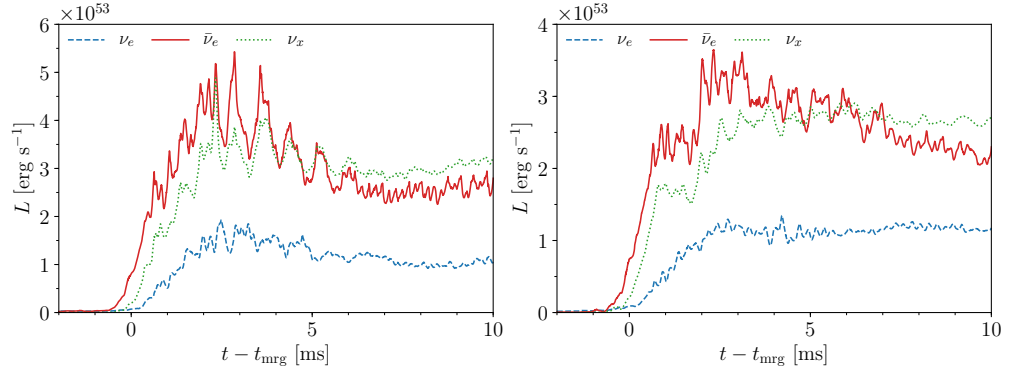


Figure 8. Neutrinos source luminosity evolution for the SFHo- ν simulation (*left panel*) and of the DD2- ν simulation (*right panel*). The electron antineutrinos have the highest luminosity until ~ 5 ms after the merger.

In Figure 9 we present the electron-flavored neutrino emissivities in the $x - y$ plane for the SFHo- ν and DD2- ν simulations. It is notable that the inner core has the smallest emissivities, which is expected from its typically high optical depth. Besides, both electron neutrinos and antineutrinos are emitted at very close rates, which amounts for a near conservation of the electron fraction shortly after the merger. Also, one notices that at specific regions of the remnant, e.g., in disk interfaces and outer portions of the spiral arms, the electron antineutrinos have emissivities that may be one order of magnitude higher than that of the electron neutrinos, which explains the luminosity dominance of electron antineutrinos over electron neutrinos in Figure 8. Besides, in the regions where the electron antineutrinos emissivity is larger than the electron neutrinos emissivity, the matter is then leptonized as visible in the lower panels of Figure 6 referring to the NLS runs. Contrary, in regions such as the outer disk, where the electron neutrinos emissivity is greater than that of the electron antineutrinos, the matter undergoes deleptonization.

5.3. Long Inspiral Simulations

Our long simulations cover ≈ 14 orbits before the merger and are performed with four different resolutions (see Table 2); cf. Appendix G for a convergence study. The quasi-circular orbit has an eccentricity of $\approx 7 \times 10^{-4}$ after applying an eccentricity reduction procedure [89,95] to the ID. In the next sections, unless stated otherwise, we use the R4 resolution. Our ID corresponds to an isentropic configuration with constant entropy per baryon equal to $s \sim 1 k_B$ and β -equilibrium.

5.3.1. Post-Merger Stage

The post-merger evolution is marked by a significant increase of the central rest-mass density over the simulations time, as depicted in Figure 5. This can be interpreted as a consequence of the phase-transition leading to the appearance of Λ hyperons at high densities,

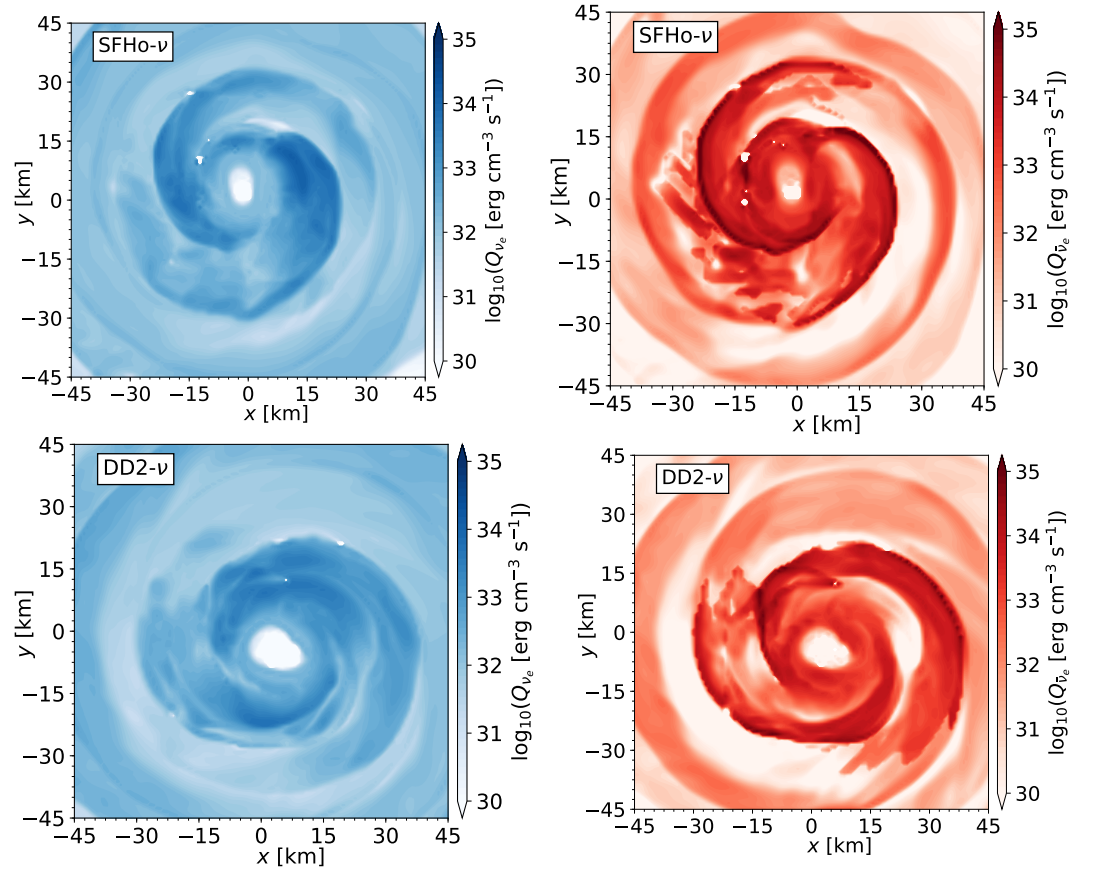


Figure 9. Effective emissivities 10 ms after the merger in the $x - y$ plane of electron neutrinos (*left panels*) and electron antineutrinos (*right panels*) for the SFHo- ν (*upper panels*) and DD2- ν (*lower panels*) runs. Here we notice that the emissions are small at the densest portion of the core, concentrate at the hot parts of the disk/spiral arms, and decreases towards the outer regions of the disk.

which, on its turn, reduces pressure support and softens the EoS. This is in accordance with the results of Ref. [97], though their results refer to cold, isothermal ID with the BHB $\Lambda\phi$ EoS.

For a better understanding of the NLS on the post-merger evolution, we show in Figure 10 snapshots of the rest-mass density, temperature, and electron fraction of our runs in the $x - y$ plane 10 ms after the merger for two cases, with and without the NLS. In the upper panels we note a remnant comprised of a massive core surrounded by a disk, which extends further for the NLS runs. In the middle panels we see that the inner core is substantially colder than the interface between the core and the surrounding disk, which is then thermally supported by higher pressure exerted by the hot material. The higher core temperature compared to that of the short inspiral simulations is reminiscent from the isentropic initial condition, by which $T_{\text{core}}(t = 0) \approx 25$ MeV and is not significantly altered during the inspiral and coalescence. In fact, the small variation of the core temperature for different EoSs is due to the general weak dependency of the pressure on the temperature for high densities. This remains true for the NLS runs because the core is also optically thick, hence neutrinos do not provide sufficient cooling within the simulation timespan. Similarly to the short inspiral runs, in the lower panels we see that the remnants are neutron-rich with $Y_e \lesssim 0.1$ at the core and the disk when neutrinos are not considered. With the NLS we observe a slight deleptonization of the core, an increase in the electron fraction at the heated arms and an overall strong deleptonization of the outer

disk regions, which can also be interpreted in light of the neutrino emissions geometry (see Section 5.3.2).

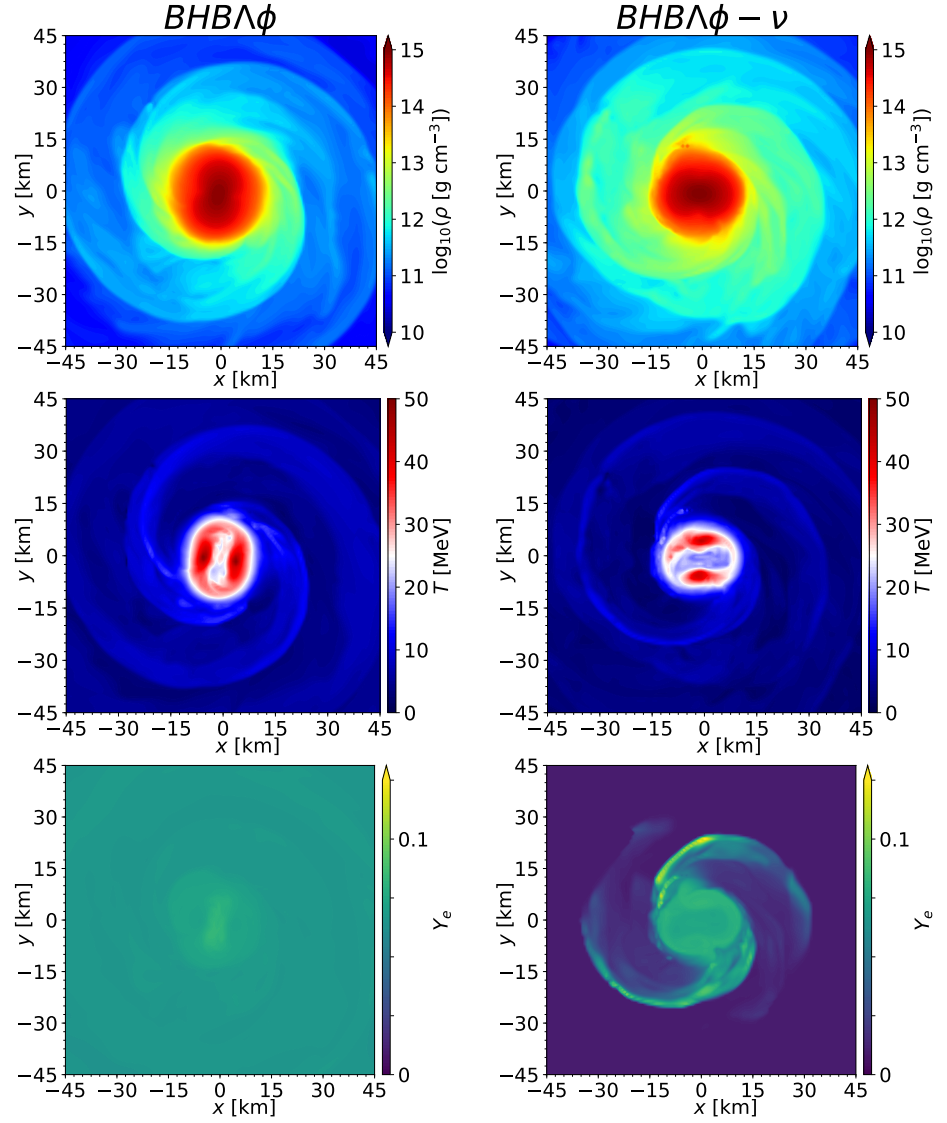


Figure 10. Snapshots of hydrodynamical quantities of the simulations $BHB\Lambda\phi$ and $BHB\Lambda\phi-\nu$ 10 ms after the merger on the $x - y$ plane. From top to bottom we have rest-mass density, temperature and electron fraction.

5.3.2. Neutrino Emissions

To the best of our knowledge, there is no previous study treating the features of a NLS implementation for an isentropic ID of the $BHB\Lambda\phi$ EoS. Therefore, in this section we present and discuss our findings and focused our comparisons on the short inspiral SFHo- ν and DD2- ν runs.

We start by presenting the luminosity evolution for the three neutrino species in Figure 11. One notices that during the late inspiral, the luminosities are greater than that of Figure 8 and may be interpreted as a consequence of the higher temperatures within the coalescing NSs with isentropic thermal profile. The appearance of luminosity peaks at $t - t_{\text{mrg}} \sim 2 - 3$ ms

followed by a decrease of the individual luminosities is similar to the behavior of Figure 11, which suggests that this emission structure is an effect of our NLS implementation rather than an EoS-dependent feature. Additionally, we note that the peak luminosities for the electron antineutrinos and heavy lepton neutrinos reach higher values than that of the short inspiral runs. However, it is difficult to point out if this is caused by the thermal profile, the employed EOS, or by the higher masses of the merging NSs. By the end of the simulation $L_{\bar{\nu}_e}$ dominates L_{ν_e} by a factor of ~ 2.2 , hence within the range obtained for the cold, low-mass SFHo and DD2 BNSs.

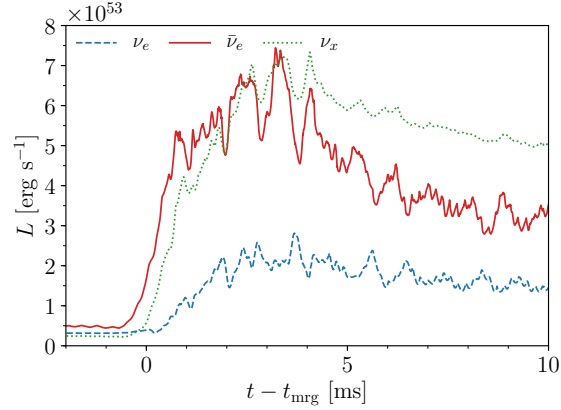


Figure 11. Neutrino luminosity evolution for the BHBA $\Delta\phi$ - ν simulation. Similarly to the short inspiral simulations, we have peak luminosities at $\sim 2 - 3$ ms after the merger, followed by a decrease towards the end of the simulation.

Likewise, the electron fraction profile of the lower right panel of Figure 10 is explained by the emission geometry depicted in Figure 12. It is interesting that the emissivities at the core of the remnant are larger than 10^{32} erg cm $^{-3}$ s $^{-1}$, which is more than two orders of magnitude higher than the counterparts for cold IDs ($< 10^{30}$ erg cm $^{-3}$ s $^{-1}$). This is due to the core temperatures $T_{\text{core}} \sim 20 - 30$ MeV reminiscent of the isentropic thermal profile of the ID. Finally, the leptonized portions of the remnant correspond to the regions where electron antineutrinos are more abundantly produced than electron neutrinos, namely at the core and the spiral arms at the inner portion of the disk. Conversely, in the remaining regions where $Q_{\nu_e} > Q_{\bar{\nu}_e}$, the fluid is deleptonized.

6. Conclusions

In this work, we presented first results of the extended infrastructure of the BAM code, with which we performed dynamical evolution of matter described by nuclear-theory based, 3-parameter EoSs and neutrinos effects via a NLS.

As a testbed of our new code framework we simulated radially-unstable TOV stars in full GR without the NLS in order to validate our GRHD implementation. This leads to a stable evolution within our simulations timespan of ~ 10 ms. A key observation regarding these tests is that the use of the high order reconstruction scheme WENOZ introduce sufficiently small numerical viscosity so that radial stability is achieved by ejection of outer material layers. We repeated these simulations with the same matter and grid configurations, but employing our NLS. We found that the NS cools and deleptonizes, and ultimately undergoes gravitational collapse in less than 10 ms.

Finally, we presented a set of BNS simulations using nuclear-theory EoSs and the NLS. In order to assess the capability of our code to handle distinct microphysical descriptions, we chose EoSs ranging from both ends of compactness, e.g., the soft SFHo and the stiff DD2, and

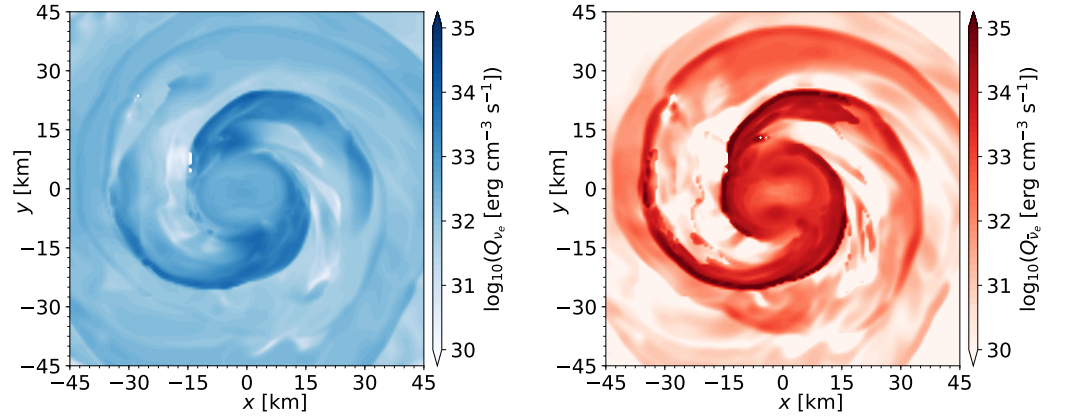


Figure 12. Effective emissivities 10 ms after the merger in the $x - y$ plane of electron neutrinos (*left panels*) and electron antineutrinos (*right panels*) for the BHB $\Lambda\phi$ - ν run. Differently than for the cold ID case, we notice that the emissivities at the core are greater as a consequence of the isentropic thermal profile, which produces temperatures of tens of MeV within the NSs. The more potent emissions are found in the outer core and along the spiral arms, mostly in the inner disk region.

including hyperons as of the BHB $\Lambda\phi$. We restricted our study to equal-mass, non-rotating systems.

Our short inspiral runs were performed with the DD2 and SFHo EoSs, with and without NLS, for the purpose of comparing results with the literature. Following Ref. [58], we consider NSs with a gravitational mass in isolation of $M = 1.2 M_{\odot}$, initially at β -equilibrium and constant temperature $T = 0.1$ MeV. Comparing our results to those of the aforementioned reference, we found good agreement in the formation of bar-like remnants that are stable during the simulations timespan, surrounded by thermally supported, thick and dense disks with pronounced spiral arms. The density and temperatures on the equatorial plane by the end of our simulations are also very to those of Ref. [58]. However, our electron fraction on the remnant is overall smaller, specially at the outer disk. This seems to be caused by our NLS implementation, in particular we may be underestimating optical depths as of Equation (43), hence predicting larger effective emission rates. This is confirmed by the peaks of total luminosity presented in Figure 8, that are larger than the peaks of Ref. [58] by a factor of two. It is worth pointing out, though, that our results are consistent in the sense that we indeed find deleptonized matter in regions where the electron neutrinos emissivities are larger than that of the electron antineutrinos, and likewise the leptonized portions of the remnant coincide with those regions at which $Q_{\bar{\nu}_e} > Q_{\nu_e}$. Also, the GWs spectra of our simulations largely agree with that of Ref. [58], reproducing similar properties.

We also performed long inspiral simulations for various grid resolutions using the BHB $\Lambda\phi$ EoS, with and without the NLS, initially with constant entropy per baryon $s \sim 1 k_B$ and in β -equilibrium. We found that the maximum rest-mass density evolution during the post-merger stage is very similar to that of Ref. [97], although they use a cold ID for this EoS, which suggests that isentropy (and consequently, the initial thermal profile) is not that relevant for the evolution of the densest portion of the remnant. The temperature at the core is not significantly altered during the inspiral and coalescence, remaining at $T_{\text{core}} \approx 25$ MeV by the end of the simulations, which is reminiscent from the initial isentropic thermal profile. Similar to the short inspiral simulations, the remnant was mostly deleptonized by the end of our simulations.

Overall, our implementations allowed long-term stable, constraint-satisfying evolutions with a performance comparable to the previous version of the BAM code (see Appendix G), despite the increase in complexity and realism encompassed by our new framework. As of Figure A14, we found that the GW phase difference of the (2, 2) decreases for increasing

resolution for the $BHB\Lambda\phi$ run, but in the case of $BHB\Lambda\phi-\nu$, there is no significant improvement by the increase of numerical resolution, which we will further investigate in the future.

Funding

This research was funded by FAPESP grant number 2019/26287-0. The simulations were performed on the national supercomputer HPE Apollo Hawk at the High Performance Computing (HPC) Center Stuttgart (HLRS) under the grant number GWanalysis/44189, on the GCS Supercomputer SuperMUC at Leibniz Supercomputing Centre (LRZ) [project pn29ba], and the HPC systems Lise/Emmy of the North German Supercomputing Alliance (HLRN) [project bbp00049].

Acknowledgements

H.G. and M.U. thank FAPESP for financial support. M.U. thanks CAPES through the Coordenação de Aperfeiçoamento de Pessoal de Nível Superior - Brasil (CAPES) - Process number: 88887.571346/2020-00 for financial support to visit the University of Potsdam during the final stages of this project, and thanks the University of Potsdam for its hospitality.

Author Contributions

Conceptualization, T.D., M.U. and H.G.; Methodology, T.D., M.U. and H.G.; Software, T.D., H.G.; Validation, H.G.; Formal Analysis, T.D., M.U., H.G. and F.S.; Investigation, T.D., M.U. and H.G.; Resources, T.D.; Data Curation, T.D. and H.G.; Writing – Original Draft Preparation, T.D., M.U., H.G. and F.S.; Writing – Review & Editing, T.D., M.U., H.G. and F.S.; Visualization, H.G.; Supervision, T.D. and M.U.; Project Administration, T.D. and M.U.; Funding Acquisition, T.D., M.U. and H.G.

Conflicts of Interest

The authors declare no conflict of interest.

1. Aasi, J.; others. Advanced LIGO. *Class. Quant. Grav.* **2015**, *32*, 074001, [arXiv:gr-qc/1411.4547]. doi:10.1088/0264-9381/32/7/074001.
2. Acernese, F.; others. Advanced Virgo: a second-generation interferometric gravitational wave detector. *Class. Quant. Grav.* **2015**, *32*, 024001, [arXiv:gr-qc/1408.3978]. doi:10.1088/0264-9381/32/2/024001.
3. Abbott, B.P.; others. GW170817: Observation of Gravitational Waves from a Binary Neutron Star Inspiral. *Physical Review Letters* **2017**, *119*, 161101, [arXiv:gr-qc/1710.05832]. doi:10.1103/PhysRevLett.119.161101.
4. Abbott, B.P.; others. Multi-messenger Observations of a Binary Neutron Star Merger. *Astrophys. J. Lett.* **2017**, *848*, L12, [arXiv:astro-ph.HE/1710.05833]. doi:10.3847/2041-8213/aa91c9.
5. Abbott, B.P.; others. Multi-messenger Observations of a Binary Neutron Star Merger. *Astrophysical Journal* **2017**, *848*, L12, [arXiv:astro-ph.HE/1710.05833]. doi:10.3847/2041-8213/aa91c9.
6. Arcavi, I.; others. Optical emission from a kilonova following a gravitational-wave-detected neutron-star merger. *Nature* **2017**, *551*, 64, [arXiv:astro-ph.HE/1710.05843]. doi:10.1038/nature24291.
7. Coulter, D.A.; others. Swope Supernova Survey 2017a (SSS17a), the Optical Counterpart to a Gravitational Wave Source. *Science* **2017**, *358*, 1556, [arXiv:astro-ph.HE/1710.05452]. doi:10.1126/science.aap9811.
8. Lipunov, V.M.; others. MASTER Optical Detection of the First LIGO/Virgo Neutron Star Binary Merger GW170817. *Astrophys. J. Lett.* **2017**, *850*, L1, [arXiv:astro-ph.HE/1710.05461]. doi:10.3847/2041-8213/aa92c0.
9. Soares-Santos, M.; others. The Electromagnetic Counterpart of the Binary Neutron Star Merger LIGO/Virgo GW170817. I. Discovery of the Optical Counterpart Using the Dark Energy Camera. *Astrophys. J. Lett.* **2017**, *848*, L16, [arXiv:astro-ph.HE/1710.05459]. doi:10.3847/2041-8213/aa9059.

10. Tanvir, N.R.; others. The Emergence of a Lanthanide-Rich Kilonova Following the Merger of Two Neutron Stars. *Astrophys. J. Lett.* **2017**, *848*, L27, [[arXiv:astro-ph.HE/1710.05455](#)]. doi:10.3847/2041-8213/aa90b6.
11. Valenti, S.; Sand, D.J.; Yang, S.; Cappellaro, E.; Tartaglia, L.; Corsi, A.; Jha, S.W.; Reichart, D.E.; Haislip, J.; Kouprianov, V. The discovery of the electromagnetic counterpart of GW170817: kilonova AT 2017gfo/DLT17ck. *Astrophys. J. Lett.* **2017**, *848*, L24, [[arXiv:astro-ph.HE/1710.05854](#)]. doi:10.3847/2041-8213/aa8edf.
12. Hajela, A.; others. Two Years of Nonthermal Emission from the Binary Neutron Star Merger GW170817: Rapid Fading of the Jet Afterglow and First Constraints on the Kilonova Fastest Ejecta. *Astrophys. J. Lett.* **2019**, *886*, L17, [[arXiv:astro-ph.HE/1909.06393](#)]. doi:10.3847/2041-8213/ab5226.
13. Hajela, A.; others. Evidence for X-Ray Emission in Excess to the Jet-afterglow Decay 3.5 yr after the Binary Neutron Star Merger GW 170817: A New Emission Component. *Astrophys. J. Lett.* **2022**, *927*, L17, [[arXiv:astro-ph.HE/2104.02070](#)]. doi:10.3847/2041-8213/ac504a.
14. Annala, E.; Gorda, T.; Kurkela, A.; Vuorinen, A. Gravitational-wave constraints on the neutron-star-matter Equation of State. *Phys. Rev. Lett.* **2018**, *120*, 172703, [[arXiv:astro-ph.HE/1711.02644](#)]. doi:10.1103/PhysRevLett.120.172703.
15. Bauswein, A.; Just, O.; Janka, H.T.; Stergioulas, N. Neutron-star radius constraints from GW170817 and future detections. *Astrophysical Journal* **2017**, *850*, L34, [[arXiv:astro-ph.HE/1710.06843](#)]. doi:10.3847/2041-8213/aa9994.
16. Fattoyev, F.J.; Piekarewicz, J.; Horowitz, C.J. Neutron Skins and Neutron Stars in the Multimessenger Era. *Phys. Rev. Lett.* **2018**, *120*, 172702, [[arXiv:nucl-th/1711.06615](#)]. doi:10.1103/PhysRevLett.120.172702.
17. Ruiz, M.; Shapiro, S.L.; Tsokaros, A. GW170817, General Relativistic Magnetohydrodynamic Simulations, and the Neutron Star Maximum Mass. *Phys. Rev. D* **2018**, *97*, 021501, [[arXiv:astro-ph.HE/1711.00473](#)]. doi:10.1103/PhysRevD.97.021501.
18. Shibata, M.; Fujibayashi, S.; Hotokezaka, K.; Kiuchi, K.; Kyutoku, K.; Sekiguchi, Y.; Tanaka, M. Modeling GW170817 based on numerical relativity and its implications. *Phys. Rev. D* **2017**, *96*, 123012, [[arXiv:astro-ph.HE/1710.07579](#)]. doi:10.1103/PhysRevD.96.123012.
19. Radice, D.; Perego, A.; Zappa, F.; Bernuzzi, S. GW170817: Joint Constraint on the Neutron Star Equation of State from Multimessenger Observations. *Astrophysical Journal* **2018**, *852*, L29, [[arXiv:astro-ph.HE/1711.03647](#)]. doi:10.3847/2041-8213/aaa402.
20. Most, E.R.; Weih, L.R.; Rezzolla, L.; Schaffner-Bielich, J. New constraints on radii and tidal deformabilities of neutron stars from GW170817. *Phys. Rev. Lett.* **2018**, *120*, 261103, [[arXiv:gr-qc/1803.00549](#)]. doi:10.1103/PhysRevLett.120.261103.
21. Tews, I.; Margueron, J.; Reddy, S. Critical examination of constraints on the equation of state of dense matter obtained from GW170817. *Phys. Rev. C* **2018**, *98*, 045804, [[arXiv:nucl-th/1804.02783](#)]. doi:10.1103/PhysRevC.98.045804.
22. Coughlin, M.W.; others. Constraints on the neutron star equation of state from AT2017gfo using radiative transfer simulations. *Mon. Not. Roy. Astron. Soc.* **2018**, *480*, 3871–3878, [[arXiv:astro-ph.HE/1805.09371](#)]. doi:10.1093/mnras/sty2174.
23. Coughlin, M.W.; Dietrich, T.; Margalit, B.; Metzger, B.D. Multimessenger Bayesian parameter inference of a binary neutron star merger. *Mon. Not. Roy. Astron. Soc.* **2019**, *489*, L91–L96, [[arXiv:astro-ph.HE/1812.04803](#)]. doi:10.1093/mnrasl/slz133.
24. Capano, C.D.; Tews, I.; Brown, S.M.; Margalit, B.; De, S.; Kumar, S.; Brown, D.A.; Krishnan, B.; Reddy, S. Stringent constraints on neutron-star radii from multimessenger observations and nuclear theory. *Nature Astron.* **2020**, *4*, 625–632, [[arXiv:astro-ph.HE/1908.10352](#)]. doi:10.1038/s41550-020-1014-6.
25. Dietrich, T.; Coughlin, M.W.; Pang, P.T.H.; Bulla, M.; Heinzel, J.; Issa, L.; Tews, I.; Antier, S. Multimessenger constraints on the neutron-star equation of state and the Hubble constant. *Science* **2020**, *370*, 1450–1453, [[arXiv:astro-ph.HE/2002.11355](#)]. doi:10.1126/science.abb4317.
26. Nedora, V.; Radice, D.; Bernuzzi, S.; Perego, A.; Daszuta, B.; Endrizzi, A.; Prakash, A.; Schianchi, F. Dynamical ejecta synchrotron emission as a possible contributor to the changing behaviour of GRB170817A afterglow. *Mon. Not. Roy. Astron. Soc.* **2021**, *506*, 5908–5915, [[arXiv:astro-ph.HE/2104.04537](#)]. doi:10.1093/mnras/stab2004.

27. Huth, S.; others. Constraining Neutron-Star Matter with Microscopic and Macroscopic Collisions **2021**. [[arXiv:nucl-th/2107.06229](#)].
28. Abbott, B.P.; others. A gravitational-wave standard siren measurement of the Hubble constant. *Nature* **2017**, *551*, 85–88, [[arXiv:astro-ph.CO/1710.05835](#)]. doi:10.1038/nature24471.
29. Guidorzi, C.; others. Improved Constraints on H_0 from a Combined Analysis of Gravitational-wave and Electromagnetic Emission from GW170817. *Astrophys. J. Lett.* **2017**, *851*, L36, [[arXiv:astro-ph.CO/1710.06426](#)]. doi:10.3847/2041-8213/aaa009.
30. Hotokezaka, K.; Nakar, E.; Gottlieb, O.; Nissanke, S.; Masuda, K.; Hallinan, G.; Mooley, K.P.; Deller, A.T. A Hubble constant measurement from superluminal motion of the jet in GW170817. *Nature Astron.* **2019**, *3*, 940–944, [[arXiv:astro-ph.CO/1806.10596](#)]. doi:10.1038/s41550-019-0820-1.
31. Coughlin, M.W.; Dietrich, T.; Heinzel, J.; Khetan, N.; Antier, S.; Bulla, M.; Christensen, N.; Coulter, D.A.; Foley, R.J. Standardizing kilonovae and their use as standard candles to measure the Hubble constant. *Phys. Rev. Res.* **2020**, *2*, 022006, [[arXiv:astro-ph.HE/1908.00889](#)]. doi:10.1103/PhysRevResearch.2.022006.
32. Pérez-García, M.A.; others. Hubble constant and nuclear equation of state from kilonova spectrophotometric light curves **2022**. [[arXiv:astro-ph.CO/2204.00022](#)].
33. Wang, H.; Giannios, D. Multimessenger parameter estimation of GW170817: from jet structure to the Hubble constant. *Astrophys. J.* **2021**, *908*, 200, [[arXiv:astro-ph.HE/2009.04427](#)]. doi:10.3847/1538-4357/abd39c.
34. Bulla, M.; Coughlin, M.W.; Dhawan, S.; Dietrich, T. Multi-messenger constraints on the Hubble constant through combination of gravitational waves, gamma-ray bursts and kilonovae from neutron star mergers **2022**. [[arXiv:astro-ph.HE/2205.09145](#)].
35. Dietrich, T.; Hinderer, T.; Samajdar, A. Interpreting Binary Neutron Star Mergers: Describing the Binary Neutron Star Dynamics, Modelling Gravitational Waveforms, and Analyzing Detections. *Gen. Rel. Grav.* **2021**, *53*, 27, [[arXiv:gr-qc/2004.02527](#)]. doi:10.1007/s10714-020-02751-6.
36. Dietrich, T.; Ujevic, M. Modeling dynamical ejecta from binary neutron star mergers and implications for electromagnetic counterparts. *Class. Quant. Grav.* **2017**, *34*, 105014, [[arXiv:gr-qc/1612.03665](#)]. doi:10.1088/1361-6382/aa6bb0.
37. Radice, D.; Perego, A.; Hotokezaka, K.; Fromm, S.A.; Bernuzzi, S.; Roberts, L.F. Binary Neutron Star Mergers: Mass Ejection, Electromagnetic Counterparts and Nucleosynthesis. *Astrophys. J.* **2018**, *869*, 130, [[arXiv:astro-ph.HE/1809.11161](#)]. doi:10.3847/1538-4357/aaf054.
38. Nedora, V.; Schianchi, F.; Bernuzzi, S.; Radice, D.; Daszuta, B.; Endrizzi, A.; Perego, A.; Prakash, A.; Zappa, F. Mapping dynamical ejecta and disk masses from numerical relativity simulations of neutron star mergers. *Class. Quant. Grav.* **2022**, *39*, 015008, [[arXiv:astro-ph.HE/2011.11110](#)]. doi:10.1088/1361-6382/ac35a8.
39. Krüger, C.J.; Foucart, F. Estimates for Disk and Ejecta Masses Produced in Compact Binary Mergers. *Phys. Rev. D* **2020**, *101*, 103002, [[arXiv:astro-ph.HE/2002.07728](#)]. doi:10.1103/PhysRevD.101.103002.
40. Metzger, B.D.; Martinez-Pinedo, G.; Darbha, S.; Quataert, E.; Arcones, A.; Kasen, D.; Thomas, R.; Nugent, P.; Panov, I.V.; Zinner, N.T. Electromagnetic Counterparts of Compact Object Mergers Powered by the Radioactive Decay of R-process Nuclei. *Mon. Not. Roy. Astron. Soc.* **2010**, *406*, 2650, [[arXiv:astro-ph.HE/1001.5029](#)]. doi:10.1111/j.1365-2966.2010.16864.x.
41. Watson, D.; others. Identification of strontium in the merger of two neutron stars. *Nature* **2019**, *574*, 497–500, [[arXiv:astro-ph.HE/1910.10510](#)]. doi:10.1038/s41586-019-1676-3.
42. Bruegmann, B.; Gonzalez, J.A.; Hannam, M.; Husa, S.; Sperhake, U.; Tichy, W. Calibration of Moving Puncture Simulations. *Physical Review D* **2008**, *77*, 024027, [[arXiv:gr-qc/gr-qc/0610128](#)]. doi:10.1103/PhysRevD.77.024027.
43. Thierfelder, M.; Bernuzzi, S.; Bruegmann, B. Numerical relativity simulations of binary neutron stars. *Physical Review D* **2011**, *84*, 044012, [[arXiv:gr-qc/1104.4751](#)]. doi:10.1103/PhysRevD.84.044012.
44. Dietrich, T.; Bernuzzi, S.; Ujevic, M.; Brüggmann, B. Numerical relativity simulations of neutron star merger remnants using conservative mesh refinement. *Physical Review D* **2015**, *91*, 124041, [[arXiv:gr-qc/1504.01266](#)]. doi:10.1103/PhysRevD.91.124041.
45. Bernuzzi, S.; Dietrich, T. Gravitational waveforms from binary neutron star mergers with high-order weighted-essentially-nonscattering schemes in numerical relativity. *Physical Review D* **2016**, *94*, 064062, [[arXiv:gr-qc/1604.07999](#)]. doi:10.1103/PhysRevD.94.064062.

46. Ruffert, M.H.; Janka, H.T.; Schaefer, G. Coalescing neutron stars: A Step towards physical models. 1: Hydrodynamic evolution and gravitational wave emission. *Astron. Astrophys.* **1996**, *311*, 532–566, [[astro-ph/9509006](#)].
47. Rosswog, S.; Liebendoerfer, M. High resolution calculations of merging neutron stars. 2: Neutrino emission. *Mon. Not. Roy. Astron. Soc.* **2003**, *342*, 673, [[astro-ph/0302301](#)]. doi:10.1046/j.1365-8711.2003.06579.x.
48. Baumgarte, T.W.; Shapiro, S.L. On the numerical integration of Einstein’s field equations. *Phys. Rev. D* **1998**, *59*, 024007, [[gr-qc/9810065](#)]. doi:10.1103/PhysRevD.59.024007.
49. Hilditch, D.; Bernuzzi, S.; Thierfelder, M.; Cao, Z.; Tichy, W.; Bruegmann, B. Compact binary evolutions with the Z4c formulation. *Phys. Rev. D* **2013**, *88*, 084057, [[arXiv:gr-qc/1212.2901](#)]. doi:10.1103/PhysRevD.88.084057.
50. Banyuls, F.; Font, J.A.; Ibanez, J.M.A.; Marti, J.M.A.; Miralles, J.A. Numerical 3+1 General Relativistic Hydrodynamics: A Local Characteristic Approach. *Astrophys. J.* **1997**, *476*, 221.
51. Read, J.S.; Lackey, B.D.; Owen, B.J.; Friedman, J.L. Constraints on a phenomenologically parameterized neutron-star equation of state. *Phys. Rev. D* **2009**, *79*, 124032, [[arXiv:astro-ph/0812.2163](#)]. doi:10.1103/PhysRevD.79.124032.
52. Shibata, M.; Taniguchi, K.; Uryu, K. Merger of binary neutron stars with realistic equations of state in full general relativity. *Phys. Rev. D* **2005**, *71*, 084021, [[gr-qc/0503119](#)]. doi:10.1103/PhysRevD.71.084021.
53. Bruenn, S.W. Stellar core collapse - Numerical model and infall epoch. *APJS* **1985**, *58*, 771–841. doi:10.1086/191056.
54. O’Connor, E.; Ott, C.D. A new open-source code for spherically symmetric stellar collapse to neutron stars and black holes. *Classical and Quantum Gravity* **2010**, *27*, 114103, [[arXiv:astro-ph.HE/0912.2393](#)]. doi:10.1088/0264-9381/27/11/114103.
55. O’Connor, E. An Open-Source Neutrino Radiation Hydrodynamics Code for Core-Collapse Supernovae. *Astrophys. J. Suppl.* **2015**, *219*, 24, [[arXiv:astro-ph.HE/1411.7058](#)]. doi:10.1088/0067-0049/219/2/24.
56. Deaton, M.B.; Duez, M.D.; Foucart, F.; O’Connor, E.; Ott, C.D.; Kidder, L.E.; Muehlberger, C.D.; Scheel, M.A.; Szilagyi, B. Black Hole-Neutron Star Mergers with a Hot Nuclear Equation of State: Outflow and Neutrino-Cooled Disk for a Low-Mass, High-Spin Case. *Astrophys. J.* **2013**, *776*, 47, [[arXiv:astro-ph.HE/1304.3384](#)]. doi:10.1088/0004-637X/776/1/47.
57. Foucart, F.; Deaton, M.B.; Duez, M.D.; O’Connor, E.; Ott, C.D.; Haas, R.; Kidder, L.E.; Pfeiffer, H.P.; Scheel, M.A.; Szilagyi, B. Neutron star-black hole mergers with a nuclear equation of state and neutrino cooling: Dependence in the binary parameters. *Phys. Rev. D* **2014**, *90*, 024026, [[arXiv:astro-ph.HE/1405.1121](#)]. doi:10.1103/PhysRevD.90.024026.
58. Foucart, F.; Haas, R.; Duez, M.D.; O’Connor, E.; Ott, C.D.; Roberts, L.; Kidder, L.E.; Lippuner, J.; Pfeiffer, H.P.; Scheel, M.A. Low mass binary neutron star mergers : gravitational waves and neutrino emission. *Phys. Rev. D* **2016**, *93*, 044019, [[arXiv:astro-ph.HE/1510.06398](#)]. doi:10.1103/PhysRevD.93.044019.
59. Neilsen, D.; Liebling, S.L.; Anderson, M.; Lehner, L.; O’Connor, E.; Palenzuela, C. Magnetized Neutron Stars With Realistic Equations of State and Neutrino Cooling. *Phys. Rev. D* **2014**, *89*, 104029, [[arXiv:gr-qc/1403.3680](#)]. doi:10.1103/PhysRevD.89.104029.
60. Shibata, M.; Kiuchi, K.; Sekiguchi, Y.; Suwa, Y. Truncated Moment Formalism for Radiation Hydrodynamics in Numerical Relativity. *Prog. Theor. Phys.* **2011**, *125*, 1255–1287, [[arXiv:astro-ph.HE/1104.3937](#)]. doi:10.1143/PTP.125.1255.
61. Cardall, C.Y.; Endeve, E.; Mezzacappa, A. Conservative 3+1 General Relativistic Boltzmann Equation. *Phys. Rev. D* **2013**, *88*, 023011, [[arXiv:astro-ph.HE/1305.0037](#)]. doi:10.1103/PhysRevD.88.023011.
62. Foucart, F.; O’Connor, E.; Roberts, L.; Duez, M.D.; Haas, R.; Kidder, L.E.; Ott, C.D.; Pfeiffer, H.P.; Scheel, M.A.; Szilagyi, B. Post-merger evolution of a neutron star-black hole binary with neutrino transport. *Phys. Rev. D* **2015**, *91*, 124021, [[arXiv:astro-ph.HE/1502.04146](#)]. doi:10.1103/PhysRevD.91.124021.
63. Anninos, P.; Fragile, P.C. Multi-frequency General Relativistic Radiation-hydrodynamics with \mathbf{M}_1 Closure. *Astrophys. J.* **2020**, *900*, 71, [[arXiv:astro-ph.IM/2007.12195](#)]. doi:10.3847/1538-4357/abab9c.

64. Foucart, F.; Duez, M.D.; Hebert, F.; Kidder, L.E.; Pfeiffer, H.P.; Scheel, M.A. Monte-Carlo neutrino transport in neutron star merger simulations. *Astrophys. J. Lett.* **2020**, *902*, L27, [[arXiv:astro-ph.HE/2008.08089](#)]. doi:10.3847/2041-8213/abbb87.
65. Weih, L.R.; Olivares, H.; Rezzolla, L. Two-moment scheme for general-relativistic radiation hydrodynamics: a systematic description and new applications. *Mon. Not. Roy. Astron. Soc.* **2020**, *495*, 2285–2304, [[arXiv:gr-qc/2003.13580](#)]. doi:10.1093/mnras/staa1297.
66. Foucart, F.; Duez, M.D.; Hebert, F.; Kidder, L.E.; Kovarik, P.; Pfeiffer, H.P.; Scheel, M.A. Implementation of Monte Carlo Transport in the General Relativistic SpEC Code. *Astrophys. J.* **2021**, *920*, 82, [[arXiv:astro-ph.HE/2103.16588](#)]. doi:10.3847/1538-4357/ac1737.
67. Radice, D.; Bernuzzi, S.; Perego, A.; Haas, R. A new moment-based general-relativistic neutrino-radiation transport code: Methods and first applications to neutron star mergers. *Mon. Not. Roy. Astron. Soc.* **2022**, *512*, 1499–1521, [[arXiv:astro-ph.HE/2111.14858](#)]. doi:10.1093/mnras/stac589.
68. Weih, L.R.; Gabbana, A.; Simeoni, D.; Rezzolla, L.; Succi, S.; Tripiccone, R. Beyond moments: relativistic Lattice-Boltzmann methods for radiative transport in computational astrophysics. *Mon. Not. Roy. Astron. Soc.* **2020**, *498*, 3374–3394, [[arXiv:physics.comp-ph/2007.05718](#)]. doi:10.1093/mnras/staa2575.
69. Perego, A.; Cabezón, R.; Käppeli, R. An advanced leakage scheme for neutrino treatment in astrophysical simulations. *Astrophys. J. Suppl.* **2016**, *223*, 22, [[arXiv:astro-ph.IM/1511.08519](#)]. doi:10.3847/0067-0049/223/2/22.
70. Gizzi, D.; O'Connor, E.; Rosswog, S.; Perego, A.; Cabezón, R.; Nativi, L. A multidimensional implementation of the Advanced Spectral neutrino Leakage scheme. *Mon. Not. Roy. Astron. Soc.* **2019**, *490*, 4211–4229, [[arXiv:astro-ph.HE/1906.11494](#)]. doi:10.1093/mnras/stz2911.
71. Gizzi, D.; Lundman, C.; O'Connor, E.; Rosswog, S.; Perego, A. Calibration of the Advanced Spectral Leakage scheme for neutron star merger simulations, and extension to smoothed-particle hydrodynamics. *Mon. Not. Roy. Astron. Soc.* **2021**, *505*, 2575–2593, [[arXiv:astro-ph.HE/2102.08882](#)]. doi:10.1093/mnras/stab1432.
72. Galeazzi, F.; Kastaun, W.; Rezzolla, L.; Font, J.A. Implementation of a simplified approach to radiative transfer in general relativity. *Phys. Rev. D* **2013**, *88*, 064009, [[arXiv:gr-qc/1306.4953](#)]. doi:10.1103/PhysRevD.88.064009.
73. Takahashi, K.; El Eid, M.; Hillebrandt, W. Beta transition rates in hot and dense matter. *Astronomy and Astrophysics* **1978**, *67*, 185–197.
74. Borges, R.; Carmona, M.; Costa, B.; Don, W.S. An improved weighted essentially non-oscillatory scheme for hyperbolic conservation laws. *Journal of Computational Physics* **2008**, *227*, 3191–3211. doi:https://doi.org/10.1016/j.jcp.2007.11.038.
75. Toro, E., *Riemann Solvers and Numerical Methods for Fluid Dynamics: A Practical Introduction*; 2009. doi:10.1007/b79761.
76. Rezzolla, L.; Zanotti, O. *Relativistic Hydrodynamics*; 2013.
77. Shen, G.; Horowitz, C.J.; Teige, S. A New Equation of State for Astrophysical Simulations. *Phys. Rev. C* **2011**, *83*, 035802, [[arXiv:astro-ph.SR/1101.3715](#)]. doi:10.1103/PhysRevC.83.035802.
78. Tolman, R.C. Static solutions of Einstein's field equations for spheres of fluid. *Phys. Rev.* **1939**, *55*, 364–373. doi:10.1103/PhysRev.55.364.
79. Friedman, J.L.; Ipser, J.R.; Sorkin, R.D. Turning point method for axisymmetric stability of rotating relativistic stars. *Astrophys. J.* **1988**, *325*, 722–724. doi:10.1086/166043.
80. Colella, P.; Woodward, P.R. The Piecewise Parabolic Method (PPM) for Gas Dynamical Simulations. *J. Comput. Phys.* **1984**, *54*, 174–201. doi:10.1016/0021-9991(84)90143-8.
81. Epstein, R.I. Lepton Driven Convection in Supernovae **1978**.
82. Steiner, A.W.; Hempel, M.; Fischer, T. Core-collapse supernova equations of state based on neutron star observations. *Astrophys. J.* **2013**, *774*, 17, [[arXiv:astro-ph.SR/1207.2184](#)]. doi:10.1088/0004-637X/774/1/17.
83. Hempel, M.; Schaffner-Bielich, J. Statistical Model for a Complete Supernova Equation of State. *Nucl. Phys. A* **2010**, *837*, 210–254, [[arXiv:nucl-th/0911.4073](#)]. doi:10.1016/j.nuclphysa.2010.02.010.
84. Banik, S.; Hempel, M.; Bandyopadhyay, D. New Hyperon Equations of State for Supernovae and Neutron Stars in Density-dependent Hadron Field Theory. *Astrophys. J. Suppl.* **2014**, *214*, 22, [[arXiv:astro-ph.HE/1404.6173](#)]. doi:10.1088/0067-0049/214/2/22.

85. Typel, S.; Oertel, M.; Klähn, T. CompOSE CompStar online supernova equations of state harmonising the concert of nuclear physics and astrophysics compose.obspm.fr. *Phys. Part. Nucl.* **2015**, *46*, 633–664, [[arXiv:astro-ph.SR/1307.5715](https://arxiv.org/abs/1307.5715)]. doi:10.1134/S1063779615040061.
86. <https://compose.obspm.fr/>.
87. Tichy, W. A New numerical method to construct binary neutron star initial data. *Classical and Quantum Gravity* **2009**, *26*, 175018, [[arXiv:gr-qc/0908.0620](https://arxiv.org/abs/gr-qc/0908.0620)]. doi:10.1088/0264-9381/26/17/175018.
88. Tichy, W. Constructing quasi-equilibrium initial data for binary neutron stars with arbitrary spins. *Physical Review D* **2012**, *86*, 064024, [[arXiv:gr-qc/1209.5336](https://arxiv.org/abs/gr-qc/1209.5336)]. doi:10.1103/PhysRevD.86.064024.
89. Dietrich, T.; Moldenhauer, N.; Johnson-McDaniel, N.K.; Bernuzzi, S.; Markakis, C.M.; Brügmann, B.; Tichy, W. Binary Neutron Stars with Generic Spin, Eccentricity, Mass ratio, and Compactness - Quasi-equilibrium Sequences and First Evolutions. *Physical Review D* **2015**, *92*, 124007, [[arXiv:gr-qc/1507.07100](https://arxiv.org/abs/gr-qc/1507.07100)]. doi:10.1103/PhysRevD.92.124007.
90. Tichy, W.; Rashti, A.; Dietrich, T.; Dudi, R.; Brügmann, B. Constructing binary neutron star initial data with high spins, high compactnesses, and high mass ratios. *Phys. Rev. D* **2019**, *100*, 124046, [[arXiv:gr-qc/1910.09690](https://arxiv.org/abs/gr-qc/1910.09690)]. doi:10.1103/PhysRevD.100.124046.
91. Wilson, J.R.; Mathews, G.J. Instabilities in Close Neutron Star Binaries. *Phys. Rev. Lett.* **1995**, *75*, 4161–4164. doi:10.1103/PhysRevLett.75.4161.
92. Wilson, J.R.; Mathews, G.J.; Marronetti, P. Relativistic numerical model for close neutron star binaries. *Phys. Rev.* **1996**, *D54*, 1317–1331, [[arXiv:gr-qc/9601017](https://arxiv.org/abs/gr-qc/9601017)]. doi:10.1103/PhysRevD.54.1317.
93. York, Jr., J.W. Conformal ‘thin sandwich’ data for the initial-value problem. *Phys. Rev. Lett.* **1999**, *82*, 1350–1353, [[arXiv:gr-qc/9810051](https://arxiv.org/abs/gr-qc/9810051)]. doi:10.1103/PhysRevLett.82.1350.
94. Hinderer, T. Tidal Love numbers of neutron stars. *Astrophys. J.* **2008**, *677*, 1216–1220, [[arXiv:astro-ph/0711.2420](https://arxiv.org/abs/astro-ph/0711.2420)]. doi:10.1086/533487.
95. Kyutoku, K.; Shibata, M.; Taniguchi, K. Reducing orbital eccentricity in initial data of binary neutron stars. *Phys. Rev. D* **2014**, *90*, 064006, [[arXiv:gr-qc/1405.6207](https://arxiv.org/abs/gr-qc/1405.6207)]. doi:10.1103/PhysRevD.90.064006.
96. Chaurasia, S.V.; Dietrich, T.; Johnson-McDaniel, N.K.; Ujevic, M.; Tichy, W.; Brügmann, B. Gravitational waves and mass ejecta from binary neutron star mergers: Effect of large eccentricities. *Physical Review D* **2018**, *98*, 104005, [[arXiv:gr-qc/1807.06857](https://arxiv.org/abs/gr-qc/1807.06857)]. doi:10.1103/PhysRevD.98.104005.
97. Radice, D.; Bernuzzi, S.; Del Pozzo, W.; Roberts, L.F.; Ott, C.D. Probing Extreme-Density Matter with Gravitational Wave Observations of Binary Neutron Star Merger Remnants. *Astrophys. J. Lett.* **2017**, *842*, L10, [[arXiv:astro-ph.HE/1612.06429](https://arxiv.org/abs/astro-ph.HE/1612.06429)]. doi:10.3847/2041-8213/aa775f.
98. Doulis, G.; Atteneder, F.; Bernuzzi, S.; Brügmann, B. Entropy-limited higher-order central scheme for neutron star merger simulations **2022**. [[arXiv:gr-qc/2202.08839](https://arxiv.org/abs/gr-qc/2202.08839)].

Appendix G Convergence of the Code

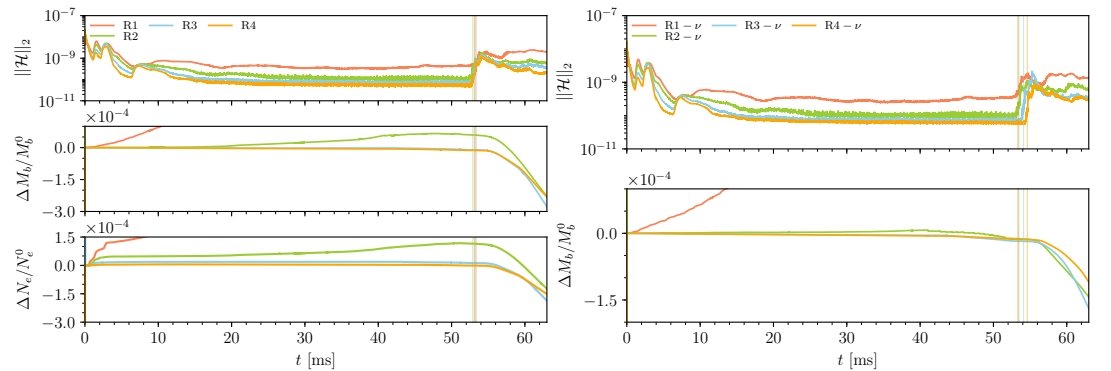


Figure A13. Constraint evolution and conserved quantities. *Left panel:* BHBA ϕ . *Right panel:* BHBA ϕ -v. We show the L_2 norm of the Hamiltonian constraint $\|\mathcal{H}\|_2$, the baryonic mass variation $\Delta M_b/M_b^0$ and the electrons number variation $\Delta N_e/N_e^0$ for the BHBA ϕ (left panel) for all four resolutions of Table 2. We observe good behavior of the Hamiltonian constraint and conserved quantities with increasing resolution in both cases. Physical quantities were extracted from the grid level $l = 1$ and the vertical lines mark the merger for each resolution.

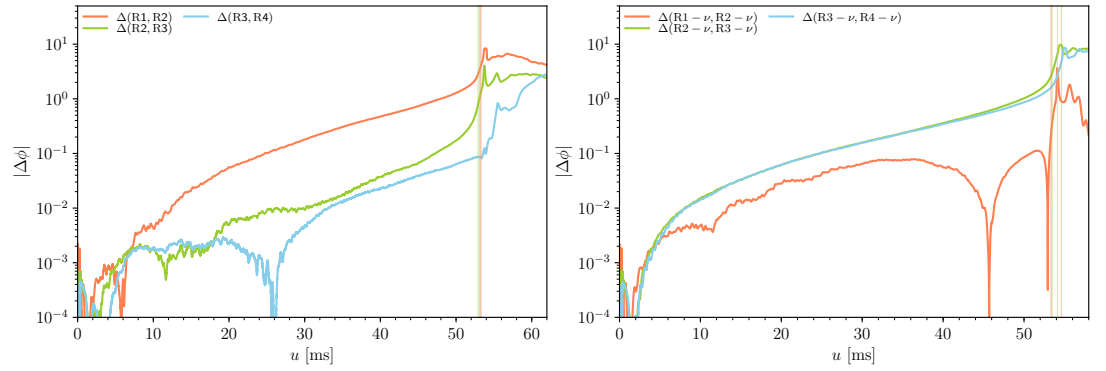


Figure A14. Phase difference of the (2,2) mode of the GW signal between different resolutions with respect to the retarded time u . The BHB $\Lambda\phi$ case is presented on the left panel and the BHB $\Lambda\phi-\nu$ case is presented on the right panel. Solid vertical lines mark the merger for each resolution.

We present in the left panel of Figure A13 the evolution of the $L2$ norm of the Hamiltonian constraint $||\mathcal{H}||_2$, the variation of the baryonic mass ΔM_b (with respect to its initial value M_b^0) and the variation of the number of electron ΔN_e (with respect to its initial value N_e^0) for the four resolutions employed for the BHB $\Lambda\phi$ EoS simulations (see Table 2). In the right panel, the same physical quantities are depicted for the BHB $\Lambda\phi-\nu$ case but not the number of electrons, which is not conserved in the implemented scheme. The behavior of the constraints and the conservation of the physical quantities improves with increasing grid resolution for both cases. For the BHB $\Lambda\phi$ case we see that for resolution R2 up to resolution R4, the Hamiltonian constraint begins at values of order $\mathcal{O}(10^{-8})$ (mainly due to the loading of the initial data), but rapidly decreases to order $\mathcal{O}(10^{-10})$ and stays at this level during the majority of the time only increasing to a stable $\leq \mathcal{O}(10^{-9})$ during the post-merger. The baryonic mass is conserved to order $\mathcal{O}(10^{-5})$ for resolutions R3 and R4, which is comparable to the results obtained when pwps are used. The conservation of the number of electrons, which was previously not included in BAM, presents small violations of order $\mathcal{O}(10^{-4})$ for resolutions R2, R3 and R4. The increase in the R2 electron number conservation violation after $t \sim 40$ ms is absent in runs R3 and R4, which suggests that this is indeed a resolution-dependent effect. For the BHB $\Lambda\phi-\nu$ case, the values of the Hamiltonian constraint stays at order $\mathcal{O}(10^{-10})$ for resolutions R3 and R4, and increase to a stable $\mathcal{O}(10^{-9})$ during the post-merger. The baryons conservation is violated to less than $\mathcal{O}(10^{-4})$ for the majority of the run and the adoption of the NLS seems to improve the behavior of the R2 resolution when compared to the BHB $\Lambda\phi$ case. In both cases we found that, after the merger, the conserved quantities accuracy is less efficient due mainly to the artificial atmosphere scheme used in BAM in which ejected material with low density is treated as atmosphere.

Overall, the results presented in Figure A13 have constraint violations of the same order when compared to simulations using the previous version of BAM [45], which relied on a simpler description of the matter using pwp EoSs.

In Figure A14, we present the convergence plots of the GW (2,2) mode phase obtained at the outermost extracted radius of the computational domain (≈ 886 km). The BHB $\Lambda\phi$ case is presented in the left and the BHB $\Lambda\phi-\nu$ case in the right panel. The difference between the phases of the R1 and R2 resolutions, $|\Delta(R1, R2)|$, is depicted for completeness because resolution R1 clearly does not conserve the physical quantities along the evolution (see Figure A13). Using the other numerical resolutions, no clear convergence order can be estimated from the plots using $|\Delta(R2, R3)|$ and $|\Delta(R3, R4)|$, and the small difference between these quantities suggests that the increasing resolution does not improve significantly the results (see for example the right panel of Figure A13 where resolutions R2, R3, and R4 give practically the same results). In

the future, we plan to employ the higher-order method outlined in [\[45\]](#) or an entropy-limited scheme such as Ref. [\[98\]](#).